Robotica (2022), **40**, pp. 3699–3725
doi:10.1017/S0263574722000509

CAMBRIDGE UNIVERSITY PRESS

RESEARCH ARTICLE

Kinematic design of a novel Multi-legged robot with Rigid-flexible coupling grippers for asteroid exploration

Qingpeng Wen, Jun He* and Feng Gao

State Key Laboratory of Mechanical Systems and Vibration, School of Mechanical Engineering, Shanghai Jiao Tong University, Shanghai 200240, China
*Corresponding author. E-mail: jhe@sjtu.edu.cn

Received: 6 September 2021; **Revised:** 10 February 2022; **Accepted:** 9 March 2022; **First published online:** 14 June 2022

Keywords: kinematic design, asteroid exploration, multi-legged robot, performance atlas, microspine

Abstract

Multi-legged robots with rigid-flexible coupling grippers have appealing applications to asteroid exploration with the microgravity. However, these robots usually have significantly complicated structures, which leads to a great challenge for the kinematic design.This paper proposes the kinematic design method for a novel multi-legged robot with the microspine gripper. First, the structure of the multi-legged asteroid exploration robot and the microspine gripper are demonstrated. Second, four performance evaluation indices, which are used to evaluate the stiffness, velocity, motion / force transfer efficiency and gripper attachment efficiency of the robot, are derived from the kinematic model. Non-dimensional design spaces of parameters to be optimized are drawn, and performance atlases are presented in design spaces. Third, the stiffness model of the microspine is derived. In addition, the constraint condition of the restoring spring is established, and the stiffness of restoring springs are optimized using the genetic algorithm. Several experiments are conducted to verify the stiffness model of the microspine. Finally, the prototype is developed and the experimental results validates the kinematic design method.

1. Introduction

Substances on the surface and inside of asteroids can help humans understand the solar system more deeply [1]. After humans completed the feat of landing on the lunar and Mars, a great deal of researchers turned their attention to the microgravity celestial bodies [2, 3]. Asteroids are thought to be aggregations of rocks, and microgravity causes it to have barely atmosphere. Near-earth asteroids are vastly small than asteroids reside in the main asteroid belt (< 1 km in diameter), and the escape velocity is usually smaller than 10 cm/s. For all that, some large rocks on rubble-pile asteroids can be anchoring sites of the asteroid robot [4].

Get benefit from the advantages of fast moving speed and wide inspection range, wheeled robots are suitable for exploration on the lunar and Mars [5, 6]. Even if the gravity is not as great as that of the earth, wheeled robots can still move on the lunar and Mars. However, the force between the wheel and the asteroid surface will make the robot escape from the asteroid. Therefore, asteroid exploration robots use other means to maintain on the surface of asteroids. The researchers have proposed three methods for robots to maintain on the surface of asteroids. First, the Philae lander fired ice bolts at Comet 67p to fix it on the surface of the asteroid [7]. The Philae lander consists of a base, an equipment platform and a polygonal sandwich structure. The immovable base that fixed on the surface of Comet 67p by ice bolts, leading it unable to locomote [8]. Therefore, the detection range of the Philae lander is limited, and the deviation between the actual landing point and the expected landing point should be as small as possible. Second, the hopping systems such as rovers on Hayabusa2 explorar has landed on the surface of the asteroid [9, 10]. An eccentric rotating rocker arm installed inside the rover is used to control the rover to jump forward or maintain on the surface of the asteroid [11]. The detection range of the hopping

systems is much larger than the Philae lander mentioned above. However, due to the small escape velocity of asteroids, the jumping height and distance of the opping systems are difficult to control. Third, the legged robots with grippers installed at the end of the leg has attracted much attention [12]. Although the moving speed of the legged robot is not as fast as the hopping system, its better body positioning ability and flexible legs enable it to walk on rugged terrain. JPL proposed a quadruped robot that can walk on the ceiling of the cave. It is also considered to be able to perform exploration missions on asteroids [13]. Kazuya Yoshida proposed a hexapod asteroid exploration robot [14]. The body of the robot is a regular hexagon, and each vertex is equipped with a 3R leg. Steel needles are installed at the end of each leg. The steel needle of the opposite leg pierces the asteroid's surface, and the robot grasps the asteroid like a gripper. Another asteroid exploration robot he proposed uses flexible ropes as legs [15]. When the robot is launched from the orbiter, its four legs curl up in a slot in the center of the fuselage. The cushioning material covering the whole fuselage can mitigate the impact during collision. Because gravity on an asteroid is negligible and terrain is rugged, hopping systems and robots with poor ability to obstacles are impossible to complete a large-scale exploration of asteroids. In order to move in microgravity, aforementioned researchers have installed grippers at the end of the legs for anchoring on the surface of the asteroid. Three types of grippers are used to assist the robot in maintaining on various planes. The first is the bionic gripper with mature technology [14, 16]. This kind of gripper usually grasps the wall through small artificial bristles like a gecko's feet. The second kind of gripper makes it firmly grasp the object surface by changing the air pressure on both sides of the foot [17]. The thired one is the Omni-directional microspine anchors provide by JPL [18]. The anchor can grasp roughnesses of rocks or walls, and the robot can walk on the ceiling of caves on Mars. The robot can utilize anchors to grasp the surface of the asteroid and locomote on the asteroid safely. Therefore, the microspine anchor have a broad prospect in asteroid exploration.

Microspines were initially taken as robots' hands that they could walk on the surface of walls or trees [19]. The technology also has applied to air vehicles and paddles for assistanting robots walking in the rocky terrain [20, 21]. The microspine technology relies on needles that grasp roughnesses of exteriors of buildings or rocks. The microspine array, arranged side by side by several flexible microspines, distribute large loads to many discrete contact points.The microspine consists of a rigid frame, a sharp hook, and elastic elements, and it is batch manufacturing using SDM technology [22]. Asbeck established the stiffness matrix of the microspine, and the physical meaning of each element in the 3×3 matrix is defined [23]. Parness analyzed necessary conditions for microspine to work normally [24]. He pointed out that the design of elastic elements is the most important for microspins, and each microspine should move independently relative to adjacent microspines to increase the possibility of all of them grasping the roughness. Wang proposed a spine mechanism to improve the shear stress [25]. Several microspine arrays share the load to enhance the maximum spine force of the spine mechanism. The load sharing system increases the compliance and reliability of the spine mechanism. Pope proposed an air vehicle that can climb on a vertical surface with microspines [26]. The perching strategy and crawling strategy of the air vehicle are discussed. He indicates that through the thrust of the rotor, the normal force of microspines and the number of roughness grasped by microspines can be increased. In a word, the research on the microspine mainly focuses on the maximum shear stress of the microspine array and broadens its application field. As Parness mentioned, the stiffness of the microspine directly affects its maximum shear stress and the probability of its hooking the surface roughness. Therefore, it is necessary to illustrate the relationship between the stiffness of the microspine and its geometric parameters. In addition, the bonding between the rigid part and the flexible part of the microspine determines its fatigue life. Adopting 3D printing technology to process two materials together is bound to increase the cost. The use of glue to stick rigid components and flexible components together will increase the workload, and it is difficult to ensure the quality of each adhesive. Therefore, it is necessary to find an alternative to the easily processed and low-cost microspines.

Considering the stiffness and pose positioning ability of the legged robot, a quadruped asteroid exploration robot is proposed in this paper. A gripper is installed at the end of each leg. The paper is organized as following: Section 2 describes the structure of the asteroid exploration robot, and introduces how the

https://doi.org/10.1017/S0263574722000509 Published online by Cambridge University Press

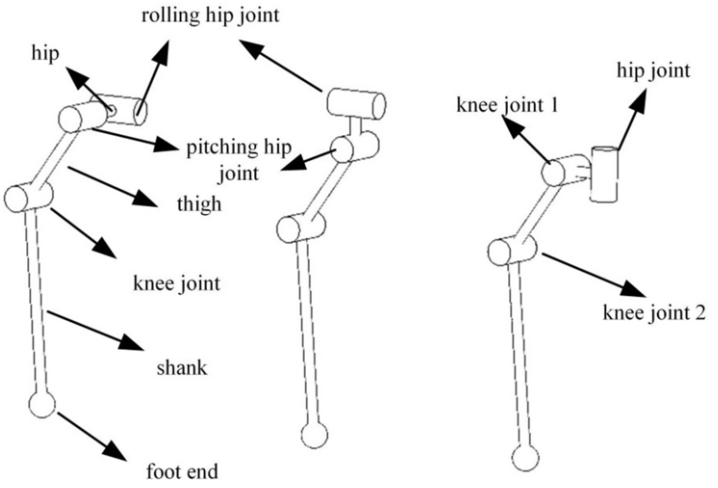

Figure 1. *Three configurations of the leg.*

rigid flexible coupling gripper works. Section 3 establishes the kinematics model, and the evaluation indices based on kinematics is deduced. Then, a novel index to evaluate the performance of the gripper is proposed. Section 4 performs the dimensional optimization of the asteroid exploration robot, and establish the stiffness of the microspine. The stiffness verification experiment of the microspine and the shear stress contrast experiment of the gripper are carried out. Finally, section 5 is the conclusion.

2. Structural description

2.1. Configuration of the leg

The traditional climbing robots have light weight and relatively simple leg structure. For example, the leg of of Dynoclimber's is 1 DOF [27], while that of Rise V3 is 2 [19]. The Lemur II has two hip joints and a knee joint [28]. This three degree of freedom leg has a large workspace in the plane of the fuselage. The working space of its knee joint is limited., which makes this robot usually regarded as a planar robot [29]. The parallel mechanism has greater stiffness and more space to install damping elements. However, the parallel legs with larger weight and more space undoubtedly increase the transportation cost. Compared with Dynoclimber and Rise V3, the three degree of freedom legs have better adaptability to terrain. 3R configurations are used with various bionic robots [30], as shown in Fig. 1. The fuselage of the robots with the first two configurations is far from the ground and has good dynamic response ability. Bionic robots such as bionic spider robots or robots transporting goods usually adopt the third configuration [31]. The fuselage of the robot with this configuration can be close to the ground, and the working space of its legs on the plane parallel to the fuselage is larger. This corresponds to demands of researchers that robots can carry out sampling operations and have good obstacle surmounting ability. Therefore, the third configuration is used as the leg of the asteroid exploration robot. For the third configuration, the servo motor of the hip joint 1 is mounted on the fuselage, and its output shaft is installed on the link of hip. Similarly, the servo motor of the first knee joint is installed on the hip, and its output shaft can drive the thigh to rotate around its axis. The servo motor of another knee joint adopts the installation method of two servo motors just before. By driving three servo motors within the specified angle range, the end of the leg can reach any position in the workspace.

2.2. Structure of the gripper

The structure of the gripper is inspired by bionics. Through the observation of cockroaches, Gregory proposed a grasping model that the force between the insect's legs and the wall usually points to the

https://doi.org/10.1017/S0263574722000509 Published online by Cambridge University Press

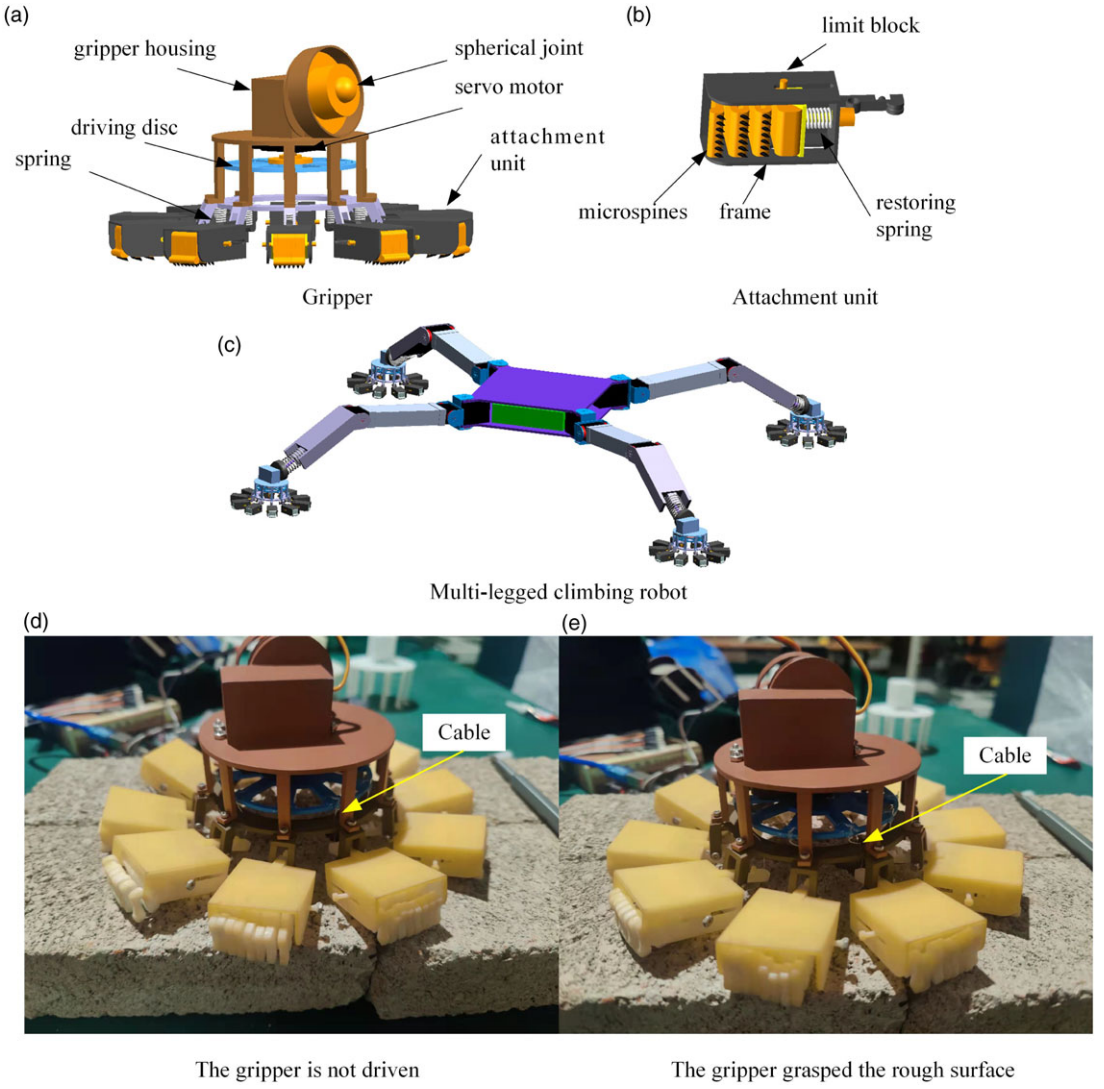

Figure 2. *Structure of the asteroid exploration robot.*

center of the body [32]. The precision and response speed of the control system should be excellent for a robot that installs a steel needle at the end of the leg and forms a gripper by penetrating into the surface of the asteroid. Because every leg lifting or body movement of the robot will cause the shear stress to deviate from the center of the body.

An omni-directional gripper is proposed to anchor the robot on the asteroid. As shown in Fig. 2, the gripper is connected to the end of the leg through a spherical joint, which improves its adaptability to the asteroid surface. The anchoring mechanism proposed by JPL is driven by gear rack. The rack converts rotational motion into linear motion. Pull the cable to drive microspines to move towards the axis of the gripper. This driving method has two disadvantages: 1) there are too many components in the driving system, which is not conducive to the lightweight of the gripper; 2) The movement of the rack will inevitably increase the height of the gripper. The gripper driven by rotation proposed in this paper attempts to solve these two problems. Attachment units are mounted on a rigid gripper housing. The attachment unit is connected with the drive disc through an inelastic cable(not shown). The rotation of

https://doi.org/10.1017/S0263574722000509 Published online by Cambridge University Press

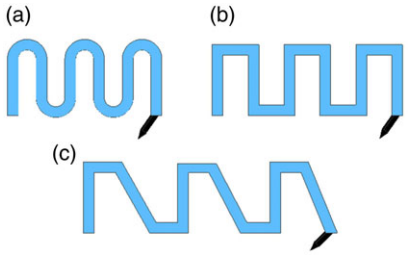

Figure 3. *Three configurations of the microspine.*

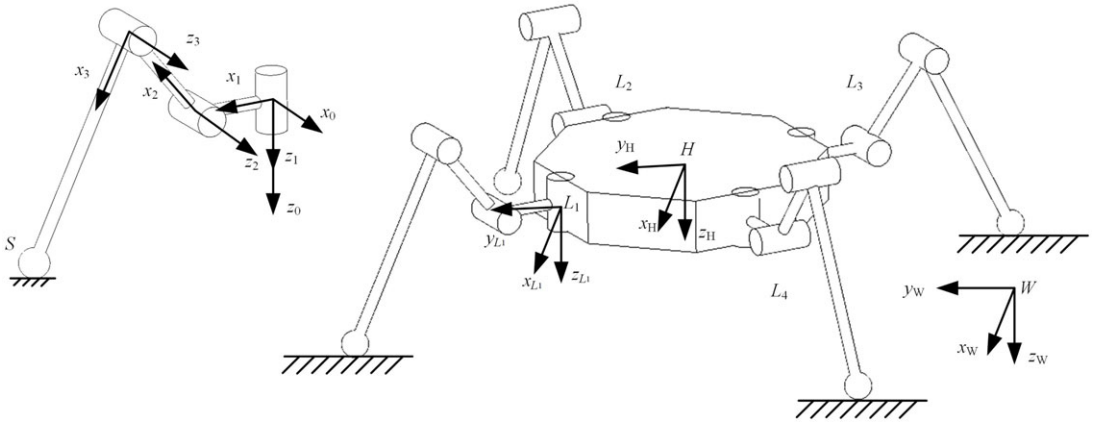

Figure 4. *Kinematic model of the multi-legged robot.*

the drive disc will pull cables, thereby driving the attachment unit to rotate around the passive rotating pair. When the driving disc returns to the initial position, attachment units also return to the initial position under the action of the restoring spring. Microspines are elastic, and the motion of microspines are relatively independent. When their base is pulled by the cable, even if some microspines grasp the ground, other microspines still have the opportunity to grasp the roughness of the ground. The function of the limit block is to prevent the microspine first grasping the ground from being damaged by the tension of the cable. The number of driving members of the gripper in this configuration is simplified. The gripper can grasp and release only through a driving member and passive springs.

Unlike the microspine proposed by Stanford University, the microspine of the asteroid robot is made of one kind of material. The shape of the microspine is changed to make it flexible. This not only reduces the processing cost, but also shortens the processing cycle of the microspine. Inspired by the spring applied in the micro electro mechanical system (MEMS), three configurations of the microspine are proposed. These three configurations can be regarded as variants of MEMS springs. Traditional MEMS springs are usually symmetrical, while the hook of the microspine is mounted on the bottom of it. Therefore, the elastic part of MEMS spring is retained and its configuration is changed appropriately. Three configurations of the microspin are proposed, as shown in Fig. 3. These configurations enable the microspine to have the similar elasticity as a cylindrical spring or a conical spring, but at the same time, it is thinner. This means that one attachment unit can hold more of the microspine.

3. Performance indices based on kinematics

3.1. Position analysis

The robot is composed of a fuselage and four identical legs. The structure of the asteroid exploration robot and coordinate systems are shown in Fig. 4. To determine the orientation of the multi-legged robot,

https://doi.org/10.1017/S0263574722000509 Published online by Cambridge University Press

Table I. *parameters.*

	α	a	θ	d
${}^{0}_{1}T$	0	0	θ_1	0
${}^{1}_{2}T$	$\frac{\pi}{2}$	l_1	θ_2	0
${}^{2}_{3}T$	0	l_2	θ_3	0

a coordinate system $\{H\}$ is attach to the center of mass of the fuselage. The z_H points to the surface of the asteroid, and y_H is along the forward direction. According to the right hand rule, the x_H axis points to the left side of the fuselage. Base coordinate systems of legs $\{L_i\}$ $(i = A, B, C, D)$ are located at hip joints of the fuselage, and D-H parameters of the leg are shown in Table I. In order to explain the absolute position and pose of the asteroid exploration robot, the world coordinate system $\{W\}$ is established.

According to parameters in Table I, the homogeneous transformation matrix can be obtain:

$$ {}^{i-1}_{i}T = \begin{bmatrix} \cos(\theta_i) & -\sin(\theta_i) & 0 & a_{i-1} \\ \sin(\theta_i)\cos(\alpha_{i-1}) & \cos(\theta_i)\cos(\alpha_{i-1}) & -\sin(\alpha_{i-1}) & -d_i\sin(\alpha_{i-1}) \\ \sin(\theta_i)\sin(\alpha_{i-1}) & \cos(\theta_i)\sin(\alpha_{i-1}) & \cos(\alpha_{i-1}) & -d_i\cos(\alpha_{i-1}) \\ 0 & 0 & 0 & 1 \end{bmatrix} \tag{1} $$

The length of the third link of the leg is the distance from the knee joint to the spherical joint, and center of spherical joint S in the knee coordinate system is: ${}^{A3}S = (l_3, 0, 0)$. In the base coordinate system of the leg 1, it can be expressed as:

$$ \begin{bmatrix} {}^{L}_{1}S \\ 1 \end{bmatrix} = {}^{0}_{1}T^{1}_{2}T^{2}_{3}T \begin{bmatrix} {}^{A_3}S \\ 1 \end{bmatrix} \tag{2} $$

Coordinates of S in the L_1 coordinate system are defined as follows according to Eq. (2):

$$ \begin{cases} [(l_1 + l_2c\theta_2) + l_3c(\theta_2 + \theta_3)]\, s\theta_1 = x \\ [(l_1 + l_2c\theta_2) + l_3c(\theta_2 + \theta_3)]\, c\theta_1 = y \\ l_2s\theta_2 + l_3s(\theta_2 + \theta_3) = z \end{cases} \tag{3} $$

where $c\theta = \cos\theta$, $s\theta = \sin\theta$. According to Eq. (3), angles of three joints can be obtained:

$$ \begin{cases} \theta_1 = \text{atan2}\left(\dfrac{y}{x}\right) \\ \theta_2 = \sin^{-1}\left(\dfrac{z}{A}\right) - \varphi \\ \theta_3 = \text{acos}\left(\dfrac{z^2 + \left(\dfrac{x}{c\theta_1} - l_1\right)^2 + \left(l_2^2 + l_3^2\right)}{2l_2l_3}\right) \end{cases} \tag{4} $$

where $A = \sqrt{l_2^2 + l_3^2 + 2l_2l_3c\theta_3}$. The other solution of θ_2, that $\theta_2 = -\pi - \sin^{-1}\left(\frac{z}{A}\right)$ exceeds the range of the joint.

Let ${}^{H}_{L}T$ denotes the rotational matrix from the base of the leg to the fuselage, ${}^{H}_{L}T$ can be express as:

$$ {}^{H}_{L}T = \begin{pmatrix} E & {}^{H}L \\ 0 & 1 \end{pmatrix} \tag{5} $$

https://doi.org/10.1017/S0263574722000509 Published online by Cambridge University Press

Let ${}^{H}L$ be the coordinates of the hip joint coordinate system in $\{H\}$, and it can be express as following:

$$ {}^{H}L = \left(R_L c\left(\frac{\pi}{4} + \frac{\pi}{2}(r-1)\right), R_L s\left(\frac{\pi}{4} + \frac{\pi}{2}(r-1)\right), z_{LH}\right)^T \ (r = 1, 2, 3, 4) \tag{6} $$

The absolute coordinates of the centroid of the fuselage is: ${}^{W}H = (H_x, H_y, H_z)^T$. The rotational matrix from $\{H\}$ to $\{W\}$ can be express as:

$$ {}^{W}_{H}T = \begin{pmatrix} {}^{W}_{H}R & {}^{W}H \\ 0 & 1 \end{pmatrix} \tag{7} $$

Therefore, the relationship between the coordinates of the spherical joint under the knee joint and the $\{W\}$ coordinate system can be expressed as:

$$ \begin{bmatrix} {}^{L}_{i}S \\ 1 \end{bmatrix} = {}^{L_I}_{H}T\,{}^{H}_{W}T \begin{bmatrix} {}^{W}S \\ 1 \end{bmatrix} \tag{8} $$

3.2. Velocity analysis

Let $\omega_i \mathcal{S}_i$ denote the velocity of the spherical joint, and the s_i point to the same direction of z_i. According to screw theory, the the velocity of the end of the leg can be express as:

$$ \omega_i \mathcal{S}_i = \omega_i S_i + \in \omega_i S_i \times r_{iP} \tag{9} $$

where r_{iP} is the vector from the origin of each coordinate system to the center of spherical joint. $\mathcal{S}_i$ can be express as:

$$ \begin{cases} \mathcal{S}_1 = (0 \quad 0 \quad 1\,;\, 0 \quad 0 \quad 0) \\ \mathcal{S}_2 = (c\theta_1 \quad -s\theta_1 \quad 0\,;\, l_1 s\theta_1 \quad l_1 c\theta_1 \quad 0) \\ \mathcal{S}_3 = (c\theta_1 \quad -s\theta_1 \quad 0\,;\, (l_2 c\theta_2 + l_1)s\theta_1 \quad (l_2 c\theta_2 + l_1)c\theta_1 \quad -l_2 s\theta_2) \end{cases} \tag{10} $$

The velocity at the center of the spherical joint can be expressed as the sum of three velocities, and it can be denoted as :

$$ \begin{bmatrix} \omega \\ v \end{bmatrix} = \begin{bmatrix} S_1 & S_2 & S_3 \\ S_1 \times r_{1P} & S_2 \times r_{2P} & S_3 \times r_{3P} \end{bmatrix} \begin{bmatrix} \dot{\theta}_1 \\ \dot{\theta}_2 \\ \dot{\theta}_3 \end{bmatrix} \tag{11} $$

By changing the coordinates of point P, the velocity of any point of the leg of the asteroid exploration robot can be obtained by Eqs. (9)–(11).

When grippers of the asteroid exploration robot grasp the ground, the multi-legged robot can be equivalent to a 4-RRR parallel platform. The velocity of the point P on the fuselage can be expressed as:

$$ V_H = \begin{bmatrix} G^O_\theta \\ G^P_\theta \end{bmatrix} \begin{bmatrix} \dot{\theta}_1 & \cdots & \dot{\theta}_n \end{bmatrix}^T \tag{12} $$

where $\left[G^O_\theta\right]_{:\,n} = S_n$ and $\left[G^P_\theta\right]_{:\,n} = S_n \times (P - R_n)$. $P - R_n$ represents the coordinate of P in the n coordinate system. For the 12 DOF system, velocities of six joints are selected as the generalized velocity. The first-order influence coefficient matrix can be expressed as:

$$ V_H = \left[G^H_\varphi\right] \dot{\varnothing} \begin{bmatrix} [G^O_\theta] \\ [G^P_\theta] \end{bmatrix} \begin{bmatrix} \dot{\varnothing}_1 & \cdots & \dot{\varnothing}_6 \end{bmatrix}^T \tag{13} $$

https://doi.org/10.1017/S0263574722000509 Published online by Cambridge University Press

3.3. Performance indices

3.3.1. Global conditioning index (GCI)

According to Section 3.2, the velocity of the asteroid exploration robot is as follows:

$$\dot{p} = J\dot{q} \tag{14}$$

where $\dot{p}$ and $\dot{q}$ are output and input velocity of the asteroid exploration robot respectively, and J is Jacobian matrix. The isotropy of the velocity transfer performance of asteroid exploration robot can be measured by the condition number index [33]. The condition number index is 1, which means that the velocity performance of the multi-legged robot is the best. From Eq. (14), we can obtain that:

$$\frac{||\delta\dot{p}||}{||\dot{p}||} \leq ||J||\,||J^{+}||\,\frac{||\delta\dot{q}||}{||\dot{q}||} = \lambda_J \frac{||\delta\dot{q}||}{||\dot{q}||} \tag{15}$$

where k is the condition number of J. The condition number can be express as:

$$k = cond\,(J) = \frac{\sigma_{max}\,(J)}{\sigma_{min}\,(J)} \tag{16}$$

where $\sigma_{max}\,(J)$ is the maximum singular values of J, and $\sigma_{min}\,(J)$ is the minimum value. The local condition index (LCI) [34] evaluates the velocity performance of robots, which is usually expressed as the reciprocal of k. The global conditioning index(GCI) used to evaluate the speed performance in the workspace is expressed as:

$$\eta_J = \frac{\int_W \frac{1}{\lambda_K} dW}{\int_W dW} \tag{17}$$

where W is the workspace of the robot.

3.3.2. Global transmission index (GTI)

Because the energy of asteroid exploration robot is limited, it is necessary to improve the energy utilization efficiency. This means that robots can detect asteroids for a longer time. The local transmission index (LTI) reflects the transmission efficiency of the robot in its workspace [35], and it is the minimum of ITI and OTI. ITI represents the efficiency between the input twist screw $\mathcal{S}_{Ii}$ (along the generalized velocity) and the transmission wrench screw $\mathcal{S}_{Ti}$. (offered by driving joints to the fuselage). OTI represents the efficiency between $\mathcal{S}_{Ti}$ and the output twist screw $\mathcal{S}_{Oi}$ (the motion of the fuselage). To evaluate the LTI in the workspace, the global transmission index(GTI) can be express as:

$$\eta_T = \frac{\int_W \min\,(\lambda_{OTI}, \lambda_{ITI})\,dW}{\int_W dW} \tag{18}$$

3.3.3. Global stiffness index (GSI)

Asteroid exploration robot should have high stiffness to resist deformation when landing and being disturbed. Obviously, stiffness is also an important index in dimensional design.

The relationship between the external force vector received by the asteroid robot and its displacement vector can be expressed as:

$$D = \begin{bmatrix} D_P \\ D_O \end{bmatrix} = J\delta q = JK^{-1}J^T \begin{bmatrix} F \\ T \end{bmatrix} \tag{19}$$

where D represents the generalized displacement vector of the asteroid exploration robot. $\begin{bmatrix} F & T \end{bmatrix}^T$ is the vector of force. Under the unit force, the deformation of the robot is as follows:

$$||D_{\max}|| = \sqrt{\max\,(|\lambda_D|)}\;||D_{\min}|| = \sqrt{\min\,(|\lambda_D|)} \tag{20}$$

https://doi.org/10.1017/S0263574722000509 Published online by Cambridge University Press

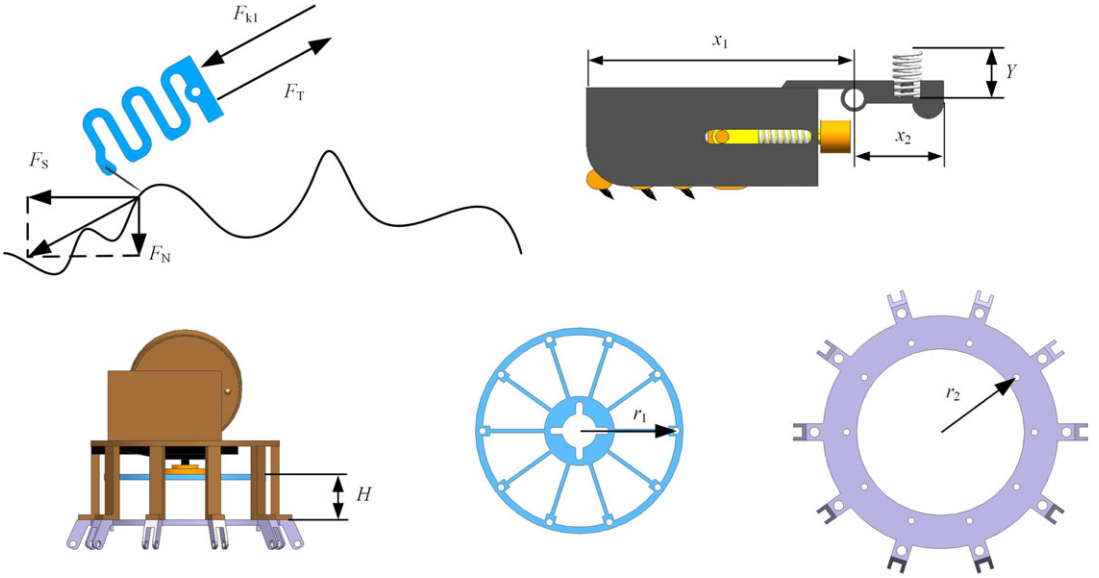

Figure 5. *Parameters of the gripper.*

where λ_D are the eigenvalues of $\left(K^{-1}\right)^T K^T$. The deformation ellipsoid that the major(minor) axis is $||D_{\max}||(||D_{\min}||)$ reflects the deformation. To evaluate the deformation of the asteroid robot in the workspace, the global stiffness index(GSI) can be obtain:

$$\eta_{s_{\max}} = \frac{\int_W ||D_{\max}||\, dW}{\int_W dW} \text{and } \eta_{s_{\min}} = \frac{\int_W ||D_{\min}||\, dW}{\int_W dW} \tag{21}$$

3.3.4. Global adhesion efficiency index (GAEI)

Gripper grasp the surface of the asteroid to anchor the asteroid exploration robot. Therefore, the gripping force should be considered first. Figure 5 shows the static model when the attachment unit grasps the roughness of the surface. The shear stress and the resultant force of F_{k_1} and F_T are opposite and equal. Neglect the influence of gravity, the static equation of the attachment unit is as follows:

$$\begin{cases} (F_T - k_1 \delta x)\cos\theta = F_f \\ T_c = F_f\,(x_1 - \delta x)\sin\theta + F_N\,(x_1 - \delta x)\cos\theta + T_s \\ T_c = F_T x_2 \cos\dfrac{\theta}{2} \\ T_s = k_2 x_2 \delta y \cos\left[\theta + \tan^{-1}\left(\dfrac{x_2\,(1-\cos\theta)}{Y - x_2\sin\theta}\right)\right] \\ \delta y = Y - \sqrt{(Y - x_2\sin\theta)^2 + [x_2\,(1-\cos\theta)]^2} \end{cases} \tag{22}$$

where k_1 and k_2 are stiffness of the spring in the attachment unit and in the vertical direction, respectively; θ ss the rotation angle of the attachment unit; Y is the length of the vertical spring; δx is the compression of the microspine and the restoring spring; T_c is the torque provided by the cable; T_s is the torque provided by the vertical spring;δy is the compression of the spring. x_1 is the length from the passive joint to the steel needle; x_2 is the distance between the passive joint and the end of the attachmeng unit. When the attachment unit of the gripper grasps the roughness of the asteroid surface, the travel of the drive disc

https://doi.org/10.1017/S0263574722000509 Published online by Cambridge University Press

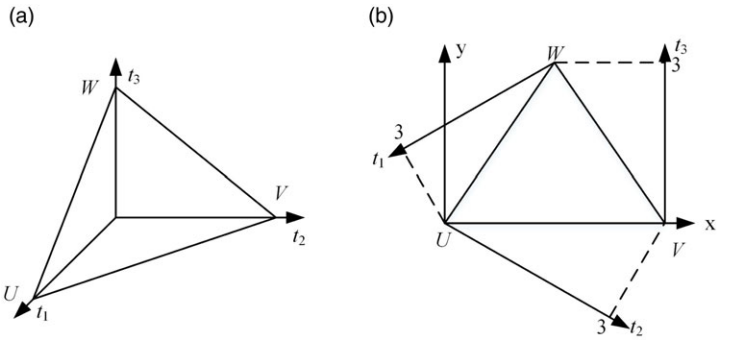

Figure 6. *Design space of the leg.*

can be obtained:

$$\theta_d = \frac{r_1^2 + r_2^2 - \left(\sqrt{(r_2 - r_1)^2 + H^2} + \delta x + \delta y\right)^2 + H^2}{2r_1 r_2} \tag{23}$$

where r_1 is the distance from the cable fixed on the drive disc to the center; r_2 is the distance from the hole on the chassis through which the cable passes to the center of the drive disc; H is the height of gripper housing. The relationship between the unit shear stress and torque provided by the drive disc can be express as:

$$\eta = \int_0^{\theta} F\left(x_1, x_2, H, Y, r_1, r_2\right) d\theta = \int_0^{\theta} \frac{\left[\left(\sin\theta + \mu\cos\theta\right) x_1 + \dfrac{\tan\theta + \mu}{k_1} + T_s\right] r_1 \cos\theta_2}{\left(x_2 \cos\dfrac{\theta}{2} + \dfrac{\sin\theta + \mu\cos\theta}{k_1}\right)\cos\theta_1} d\theta \tag{24}$$

where $\theta_1 = \dfrac{\pi}{2} - \theta - \theta_d$, and $\theta_2 = \tan^{-1}\dfrac{H\sin\theta_d}{r_2 - r_1\cos\theta_d}$.

4. Dimension and stiffness design

The main purpose of this section is to optimize the performance of asteroid exploration robot by optimizing dimensional parameters.

4.1. Dimensional design

The essence of dimension design is to find the appropriate proportion of dimensions to optimize the performance of the robot. l_1, l_2 and l_3 are normalized:

$$\frac{1}{3}\left(l_1 + l_2 + l_3\right) = L \tag{25}$$

Non-dimensional parameters can be obtained as follows:

$$t_1 + t_2 + t_3 = 3 \tag{26}$$

where t_i $(i = 1, 2, 3)$ are non-dimensional parameters. They are expressed by an orthogonal coordinate system, as shown in Fig. 6(a). Since all parameters are positive, these parameters are always in the triangular δUVW. In order to analyze the impact of a single parameter on performance, three-dimensional parameters are projected into a two-dimensional plane, as shown in Fig. 6(b).

Dimensions of the robot fuselage l_p, the length of its legs l_{leg} and the support polygon l_b when standing affect its stiffness and velocity. As with the previous method, non-dimensional parameters are obtained:

https://doi.org/10.1017/S0263574722000509 Published online by Cambridge University Press

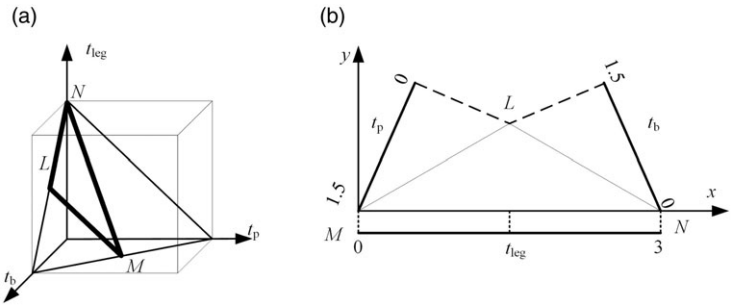

Figure 7. *Design space of the multi-legged robot.*

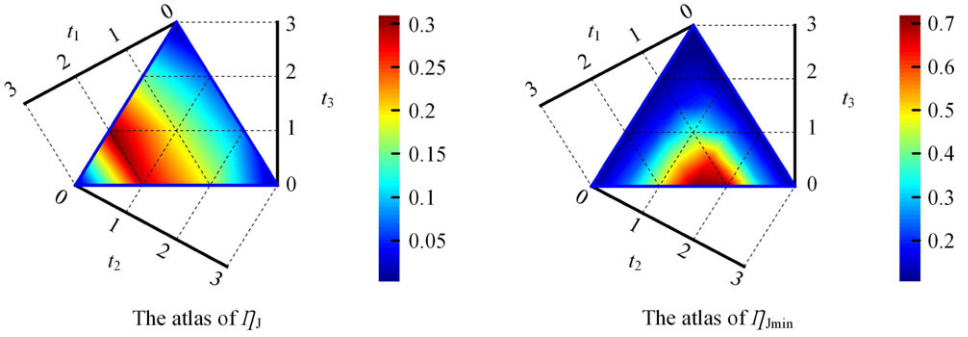

Figure 8. *GCI atlas of the leg.*

$$\frac{1}{3}\left(l_p + l_b + l_{leg}\right) = L \tag{27}$$

The sum of non-dimensional parameters can be expressed as:

$$t_p + t_b + t_{leg} = 3 \tag{28}$$

where t_p, t_b and t_{leg} are non-dimensional parameters. In addition to positive numbers, non-dimensional parameters also need to meet the following geometric constraints::

$$\begin{cases} 0 < t_p, t_b, t_{leg} < 3 \\ t_p < t_b \\ t_b < t_p + t_{leg} \end{cases} \tag{29}$$

The parameter space is shown in Fig. 7(a). After coordinate transformation, the parameter space δLMN is shown in Fig. 7(b).

The combination of non-dimensional parameters in the red area means that the performance of the asteroid exploration robot is excellent. As can be seen from Fig. 8: (1) η_J gradually decreases from the maximum value as t_1 changes from 2 to 0 or 3. (2) The red area in Fig. 8(a) is located where t_2 and t_3 is less than 1.8. (3) t_1 and t_2 have similar effects on $\eta_{J_{\min}}$. When t_1 or t_2 is 1.5, $\eta_{J_{\min}}$ reaches the maximum value. Their increase or decrease will cause the decrease of $\eta_{J_{\min}}$. (4) The closer t_3 is to 0, the greater $\eta_{J_{\min}}$ is. (5) The Red areas of the two performance atlases coincide with t_1 and t_2, ranging from 0.8 to 2.2. Therefore, the optimization space of non-dimensional parameters is: $\omega_J = \{(t_1, t_2, t_3) | 1.2 < t_1 < 2.2, 0.8 < t_2 < 1.8)\}$

Figure 9 illustrates the effect of dimensionless parameters on η_S and $\eta_{S_{\min}}$. As shown in Fig. 9 that: (1) The high-performance region in Fig. 9(a) is included in Fig. 9(b). This means that the parameter

https://doi.org/10.1017/S0263574722000509 Published online by Cambridge University Press

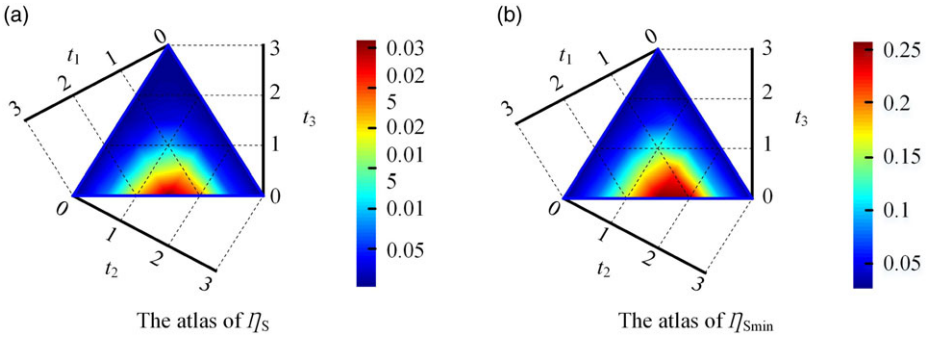

Figure 9. *GSI atlas of the leg.*

combination that makes η_S performance excellent also makes $\eta_{S_{\min}}$ performance excellent. Therefore, we only focus on the parameter combination that makes η_S excellent. (2) Obviously, t_1 and t_2 have similar effects on η_S. When t_1 and t_2 are in the middle of the parameter space, η_S reaches the maximum. When t_1 and t_2 are close to the extreme point of the parameter space, η_S reaches the minimum value. (3) The value of η_S is inversely proportional to the proportion of t_3. It means reducing t_3, which helps to improve the stiffness of the asteroid exploration robot. In a word, when the parameter combination is located at the midpoint of the bottom edge of the parameter space δUVW, the leg deforms less under the action of external force. Therefore, the optimization space of non-dimensional parameters is: $\omega_S = \{(t_1, t_2, t_3)|0.8 < t_1 < 2.1, 1.2 < t_2 < 2, 0 < t_3 < 1)\}$.

In order to ensure the safety of asteroid robot, quasi-static gait is adopted. When the fuselage moves, it should be ensured that the four legged grippers grasp the surface of the asteroid. Similarly, the asteroid exploration robot should keep all grippers anchored on the asteroid surface during sampling and other operations. Therefore, it is assumed that the four legs of the robot are standing on the surface of the asteroid when discussing the dimensional optimization of the robot. Above two performance atlases illustrate the influence trend of three parameters to be optimized on the kinematics based performance of the leg. In summary, when the parameter combination is located in the middle and lower of the parameter space triangle, the legs of the asteroid exploration robot have better kinematic performance. Obviously, when the parameter combination is located at the intersection of a and B, both velocity and stiffness performance are considered. The non-dimensional parameters design space of the leg can be obtain: $\omega_{LEG} = \{(t_1, t_2, t_3)|0.8 < t_1 < 2, 0.8 < t_2 < 1.8, 0 < t_3 < 1)\}$

Next, the dimensional design of the robot is discussed. Four performance atlases in Fig. 10 reflect the influence of non-dimensional parameters of the robot on performance of linear velocity and angular velocity. It can be seen from the Fig. 10 that: (1) The red region in $\eta_{P_{\max}}$ is included in the red region in $\eta_{P_{\min}}$, and three dimensionless parameters have similar effects on both $\eta_{P_{\max}}$ and $\eta_{P_{\min}}$. (2) Take $\eta_{P_{\max}}$ as an example, $\eta_{P_{\max}}$ increases monotonically with the increase of t_b, and decreases monotonically with the increase of t_p. (3) $\eta_{P_{\max}}$ reaches the maximum value when t_{leg} is near the midpoint of dimensional space, and the closer t_{leg} is to the extreme point, the smaller $\eta_{P_{\max}}$ is. (4) The red area in Fig. 10(c) is located at the top right of the design space, which means that larger t_{leg} and t_b and smaller t_p make the performance of $\eta_{o_{\min}}$ better. (5) $\eta_{o_{\max}}$ increases monotonically with the increase of t_b, and decreases monotonically with the increase of t_p. The value of $\eta_{o_{\max}}$ is greater when t_{leg} is in the range of 0.75 to 2. In general, red areas of performance atlases are located in the middle of the triangle of the design space. Therefore, the non-dimensional parameters design space based on velocity performance is as follows: $\omega_{KR} = \{(t_p, t_b, t_{leg})|0 < t_p < 1.2, 0.75 < t_b < 1.5, 0.75 < t_{leg} < 2)\}$.

Four performance atlases in Fig. 11 reflect the influence of non-dimensional parameters of the robot on performance of linear stiffness and angular stiffness. It can be seen from Fig. 11 that: (1) $\mu_{P_{\min}}$ almost monotonically increases with the increase of t_b, and it reaches the maximum value when t_b is about 1.2. (2) The value of $\mu_{P_{\min}}$ is negatively correlated with the value of t_p, that is, appropriately reducing t_p

https://doi.org/10.1017/S0263574722000509 Published online by Cambridge University Press

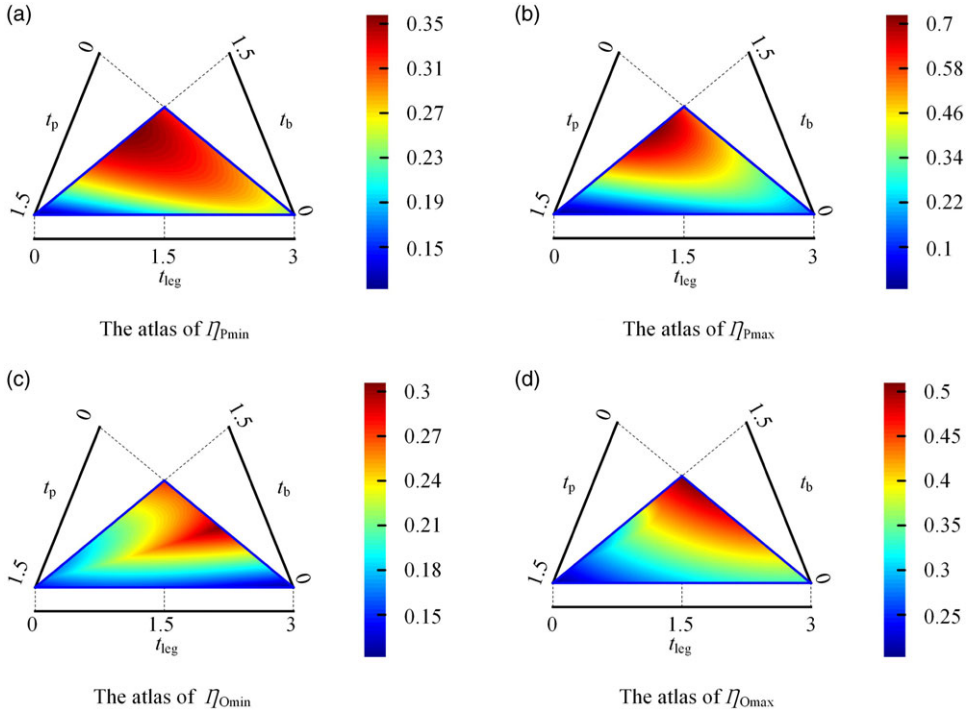

Figure 10. *GCI atlas of the robot.*

is conducive to improving $\mu_{P_{\min}}$. (3) Properly increasing t_{leg} will help to improve $\mu_{P_{\min}}$. However, if t_{leg} exceeds 2.5, $\mu_{P_{\min}}$ decreases with the increase of t_{leg}. (4) The effects of t_p and t_{leg} on $\mu_{P_{\max}}$ are similar to their effects on $\mu_{P_{\min}}$. For t_b, its value is maintained around 0.75, which is conducive to improving $\mu_{P_{\max}}$. (5) When t_b is greater than 1 or t_p is less than 1.2, the value of $\mu_{O_{\min}}$ is greater. When t_{leg} is near 1.2, the value of $\mu_{O_{\min}}$ is greater, and the closer t_{leg} is to the extreme point, the smaller $\mu_{O_{\min}}$ is. (6) Smallert_b and t_{leg} help to improve $\mu_{O_{\max}}$, while $\mu_{O_{\max}}$ is negatively correlated with t_p. In a word, red areas of the four performance atlases are located in the upper right, upper left and lower left of the design space respectively. This means that it is difficult to find a set of non-dimensional parameters to make the four properties excellent at the same time. When selecting dimensionless parameters, a certain performance will be ignored or the four performances will be relatively moderate. In this paper, $\mu_{P_{\max}}$ and $\mu_{O_{\max}}$ are given priority because they reflect the maximum deformation of the asteroid exploration robot when receiving an external force. Therefore, the non-dimensional parameters design space based on stiffness performance is as follows:$\omega_{SR} = \{(t_p, t_b, t_{leg})|0 < t_p < 0.6, 0.55 < t_b < 1.5, 1 < t_{leg} < 2.5)\}$.

In order to verify the stiffness performance of the asteroid exploration robot, a simulation was performed. The configuration and posture of the robot is shown in Fig. 12.

The joint angle error of the leg of the asteroid exploration robot is random, and the Euclidean length of the column vector composed of the errors of the three joints is 1. In order to fully evaluate the stiffness performance of the robot, the leg and robot are simulated 20 times respectively. The stiffness performance of the legs and robot dimensions of the asteroid exploration robot before and after optimization is shown in Fig. 13(a) and Fig. 13(b)–(c).

As can be seen from Fig. 13(a), the stiffness of the leg of the asteroid exploration robot has been significantly improved after dimensional optimization. In the face of possible joint errors, the stiffness of the leg is increased by 16.96%. When measuring the stiffness performance of the robot, positions of spherical joints are fixed. The second norm of the error of all joints is 1. Figure 13(b) shows the position deviation of the fuselage of the asteroid exploration robot when there are errors in joint angles.

https://doi.org/10.1017/S0263574722000509 Published online by Cambridge University Press

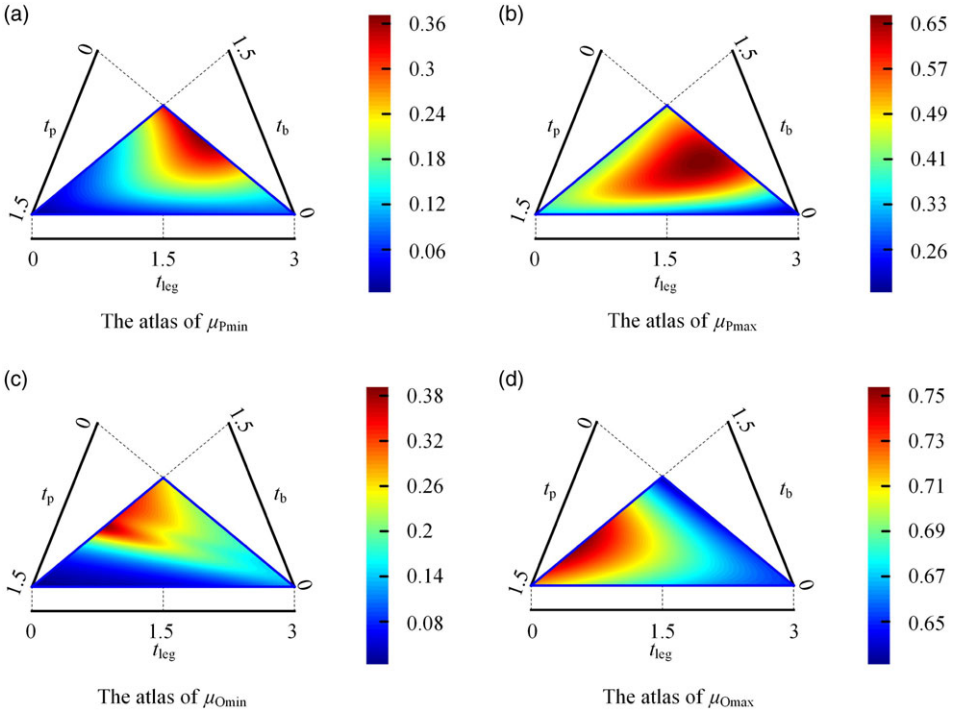

Figure 11. *GSI atlas of the robot.*

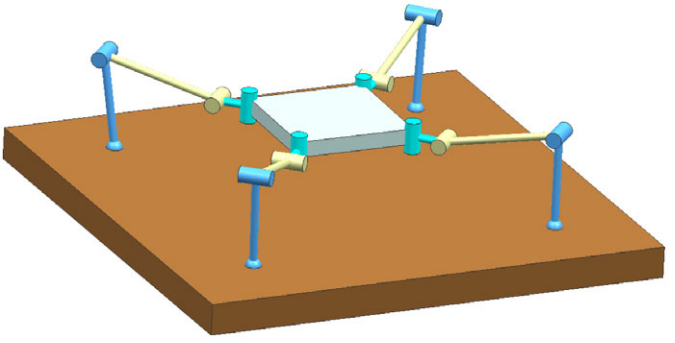

Figure 12. *The configuration and posture of the robot.*

As can be seen from the figure, the position deviation of the fuselage has been significantly reduced after dimensional optimization. The calculation shows that the position deviation is reduced by 19.65%. Errors of roll angle and pitch angle are also reduced by 8.25% and 18.7% respectively compared with those before dimensional optimization.

Performance atlase in Fig. 14 reflects the influence of non-dimensional parameters of the robot on GTI performance. The following features can be obtained: (1) The high GTI performance area is located near the bottom edge of the triangle in the parametric design space. (2) η_{GTI} increases monotonically with the increase of t_b. This means that a larger t_b helps improve η_{GTI}. (3) The effect of t_p on η_{GTI} is opposite to that of t_b. That is, a smaller t_p helps to improve η_{GTI}. (4) t_{leg} located in the center of the design space helps to improve the performance of η_{GTI}. Based on the above analysis, the non-dimensional parameters design space based on GTI performance can be obtain: $\omega_{GTI} = \{(t_p, t_b, t_{leg}) | 0.2 < t_p < 0.8, 0.6 < t_b < 1.3, 0.7 < t_{leg} < 2.2)\}$

https://doi.org/10.1017/S0263574722000509 Published online by Cambridge University Press

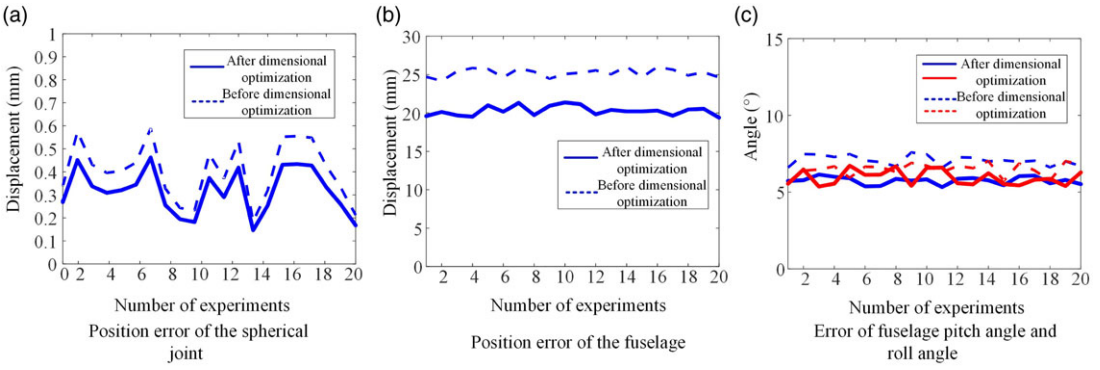

Figure 13. *The stiffness performance of the legs and robot. (c) The middle red curve represents the pitching angle of the asteroid detection robot, and the blue curve represents the rolling angle of the asteroid detection robot.*

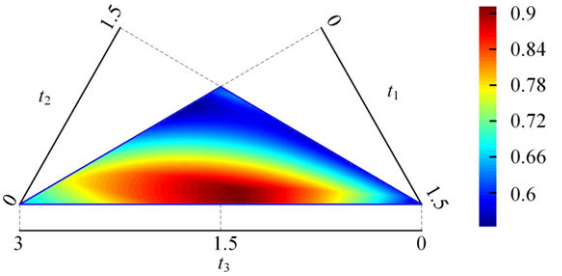

Figure 14. *GTI atlas of the robot.*

Figures 10–14 show the performance atlas of the asteroid exploration robot. By analyzing each group of performance atlas, the corresponding design space is obtained. By finding the intersection of all design spaces, the optimal design space of the asteroid exploration robot can be obtained:

$$\omega_{ROBOT} = \left\{ \left(t_p, t_b, t_{leg}\right) \left| 0.2 < t_p < 0.6, 0.75 < t_b < 1.2, 1 < t_{leg} < 2.2 \right) \right\} \tag{30}$$

Based on the optimization results, we are able to design the asteroid robot. According the optimization results, $t_1 : t_2 : t_3 : t_p : t_b = 1.2 : 1.4 : 0.4 : 1.5 : 2$ is a set of candidate solution. These parameters are dimensionless, so corresponding parameters can be obtained by multiplying a dimension coefficient X. Let the dimension coefficient X = 100 mm, we can obtain $t_1 = 120$ mm, $t_2 = 140$ mm, $t_3 = 40$ mm, $t_p = 150$ mm.

The performance atlas method can be used for the robot's dimensional optimization. Is benefits from a hierarchical optimization. Dimensions of the leg are optimized primarily, and then the optimized leg and fuselage are optimized. The five parameters are divided into two groups and optimized respectively. For global adhesion efficiency index, there are six parameters need to be optimized. It is difficult to project all parameters onto a performance map book through coordinate transformation. The intelligent algorithm can effectively solve the problem of multi parameter optimization. Genetic algorithm is an intelligent algorithm to solve the multi parameter optimization problem. The optimal solution is found by imitating the selection and genetic mechanism of nature. Genetic algorithm is used to guide the parameter optimization of gripper. It is assumed that the stiffness of the two springs constitutes an identity matrix. The workspace of the passive joint is 30 °. GAEI can be written as:

$$F = f\left(x_1, x_2, H, Y, r_1, r_2\right) \tag{31}$$

https://doi.org/10.1017/S0263574722000509 Published online by Cambridge University Press

Table II. *Optimal parameters of the gripper.*

Parameters	r_1	r_2	Y	H	x_1	x_2
Value	0.5899	0.5945	0.5309	0.8856	0.9992	0.9701

Table III. *Geometric parameters of five gripper prototypes.*

Number	$r_1(r_2)$	Y	H	x_1	x_2
a	$1.2r_1(r_2)$	Y	H	x_1	x_2
b	$r_1(r_2)$	Y	$1.5H$	x_1	x_2
c	$r_1(r_2)$	$1.5Y$	H	x_1	x_2
d	$r_1(r_2)$	Y	H	x_1	$1.2x_2$
e	$r_1(r_2)$	Y	H	$1.2x_1$	x_2

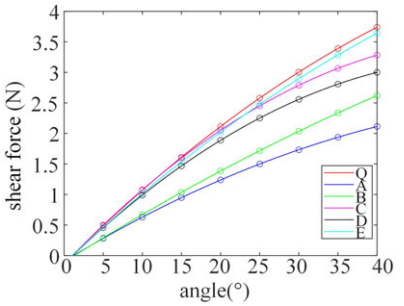

Figure 15. *The relationship between the angle of servo motor and driving force.*

The following geometric constraints should be considered in parameter optimization.

$$\begin{cases} r_1 < r_2 \\ x_2 \sin\theta < Y \\ x_1, x_2, H, Y, r_1, r_2 > 0 \end{cases} \tag{32}$$

The randomness of the optimization process of genetic algorithm leads to different optimization results. Therefore, ten optimization results are selected and the average value is obtained. The optimization results are shown in Table II.

In order to verify whether the design of dimensional parameters of the gripper is appropriate, several grippers with different geometric parameters are machined. Only one parameter of each gripper is properly adjusted. Parameters of each gripper are shown in Table III.

The adhesion test results of all grippers are shown in Fig. 15. Where Q is the experimental data of the gripper without parameter adjustment. It can be seen from the figure that r_1 has the greatest influence on the adhesion, followed by H. The adhesion was 0.5640 and 0.7033 times of that of the conventional gripper. Y and x_2 have lower effect on the adhesion, and the adhesion is 0.8722 and 0.7969 times of that of the gripper Q, respectively. The influence of x_1 on the adhesion is the smallest, which is 0.9737 times of that of the conventional size.

4.2. Stiffness design

The microspine array contains multiple microspines, as shown in Fig. 16. The microspine is like a plane spring, so the movement of microspines does not affect each other. The microspine in the red circle

https://doi.org/10.1017/S0263574722000509 Published online by Cambridge University Press

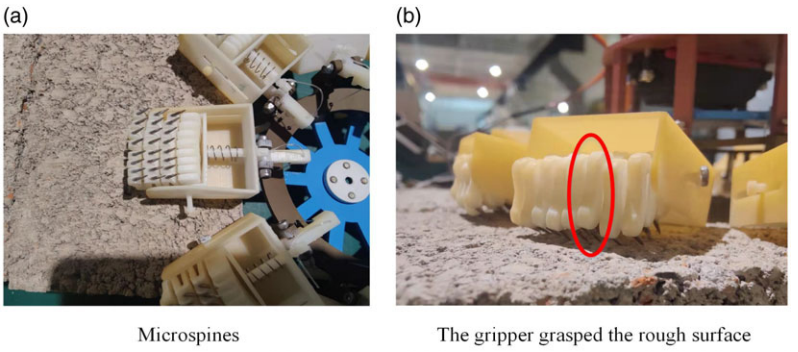

Figure 16. *Structure of the microspine.*

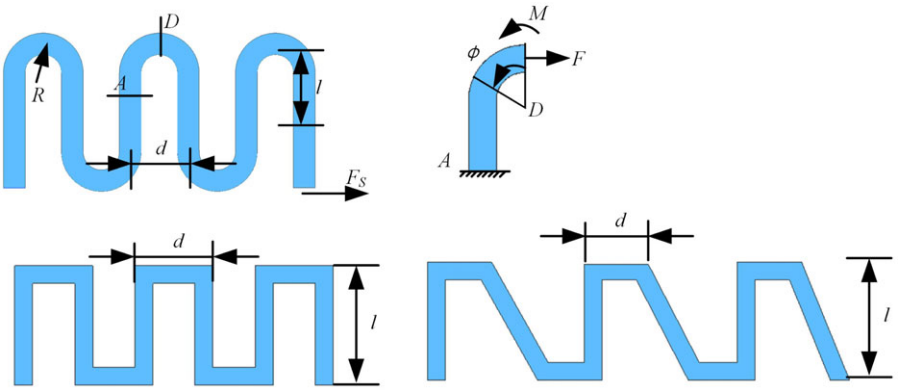

Figure 17. *The structural and parameters of the microspine.*

first grasp the ground, and other microspines still have the opportunity to grasp the rough surface. The purpose of the attachment unit is to group all microspines. Since the load is distributed to each attachment unit, a larger number of attachment units undoubtedly reduce the load borne by each attachment unit.

Structural parameters of the microspine are shown in Fig. 17. Taking configuration (a) as an example, the microspine is designed to be snake shaped, which makes it flexible. The microspine can be simplified into several components with the same structure. One of the basic elements is taken for analysis, and its deformation is assumed to be in the linear range. Suppose the left end of the microspine is fixed and a force points to right is applied to the right end. a is the width of the cross section, d is the spacing, b is the thickness of the microspine, l is the height of the microspine, and R is the radius of the semicircle arc.

Considering the symmetry of the microspine,, the axial force of section D can be obtained: $F = 0.5F_S$. The shear stress is zero and the bending moment is M. Rotation angles of these sections are both zero. Therefore, a static basis with fixed section A and free end section D can be established. φ is the angle between a section of circular arc structure and the vertical direction. The bending moment of each section of the arc part can be expressed as:

$$\begin{cases} M(\varphi) = M - FR(1 - \cos\varphi) \\ \dfrac{\partial M(\varphi)}{\partial M} = 1 \end{cases} \tag{33}$$

https://doi.org/10.1017/S0263574722000509 Published online by Cambridge University Press

The bending moment of each section of the straight line can be expressed as:

$$\begin{cases} M(x) = M - FR(R + x) \\ \dfrac{\partial M(x)}{\partial M} = 1 \end{cases} \tag{34}$$

According to the deformation compatibility condition, the rotation angle θ of section D is 0, and θ is the angle produced by the rotation of the beam section around the neutral axis under the action of bending moment. According to Karnofsky's second theorem:

$$\theta = \frac{1}{EI}\left(\int_0^{\frac{\pi}{2}} M(\varphi)\frac{\partial M(\varphi)}{\partial M} Rd\varphi \int_0^l M(x)\frac{\partial M(x)}{\partial M} dx\right) = 0 \tag{35}$$

The result is as follows:

$$M = F\frac{l^2 + 2Rl + \pi R^2 + 2R^2}{2\pi R + 4l} \tag{36}$$

where E is the elastic modulus of the material used for the microspine. The deformation of the microspine δ can be obtained by introducing M into $M(\varphi)$ and $M(x)$ by Karnofsky's second theorem. The stiffness of the microspine can be expressed as:

$$k_a = \frac{F}{\delta} = \frac{24EI}{40l^3 + 5R\pi a^2 + 144lR^2 + 12\pi R^3 + 64R^3} \tag{37}$$

Similarly, the stiffness of configuration (b) and configuration (c) can be obtained:

$$k_b = \frac{12EI}{20l^3 + 36l^2d + 3a^2d} \text{ and } k_c = \frac{F_x}{\delta_x} = \frac{12EI}{8l^3 + 36l^2d + 3a^2d + \dfrac{12l^3}{sin\alpha}} \tag{38}$$

In order to verify the stiffness formula, CAE simulation of the microspine is carried out. The left end of the microspine is fixed and subjected to a friction force of 1, 1.5, 2, 2.5, 3, 3.5, 4, 4.5, 5N. Geometric parameters of the microspine are as follows: $l_a = l_b = l_c = 10$, $R_a = 4$, $d_b = 9$, $\alpha = 44.5°$ and $E = 3000$ MPa. Bring these parameters into Eq. (37) and (38), and the stiffness of the microspine is shown in Fig. 18. The figure illustrates that the stiffness of configuration (c) is the largest and that of configuration (a) is the smallest under the same cross-sectional area parameters. Smaller stiffness tends to increase the probability that the microspine catches the roughness of the surface of asteroids. In order to enhance the adaptability of the gripper to the asteroid surface, configuration (a) is chosen as the microspine.

The microspine is the most important component of the gripper, and the stiffness model of the microspine should be verified. The micropine is resin processed, which not only ensures its quality, but also reduces the weight of the gripper. In practical application, the microspine can withstand a tensile force of 10N without plastic deformation. The hook of the microspine grasps the edge of the fix platform and the attachment unit is pulled in the direction of the arrow. The tension and displacement are recorded and used to calculate the stiffness of the microspine. The geometric parameters and material properties of the microspine are as follows: $b = 1.5$, $h = 2.5$, $R = 2.5$, $l = 6.5$ and $E = 3780$ MPa. The relationship between the tensile force and the deformation of the microspine is shown in Fig. 19(b). It can be seen from the figure that the curve calculated theoretically coincides with the curve measured practically, and the stiffness model of the microspine is proved to be correct.

After the stiffness model of the microspine is established, its stiffness and the stiffness of the restoring spring need to be optimized. Suppose that when the microspine contacts the surface of the asteroid, it immediately contacts the roughness. It can be called immediate grasping mode. If the microspine needs to be pulled by the cable to grasp the roughness, this situation can be called pulling grasping mode. Obviously, catching other roughness after the micropine detachments also belongs to pulling grasping mode. The stiffness of the microspine and the restoring spring should be designed separately for above two kinds of grasping modes of the microspine. For the immediate grasping mode, the main function of the restoring spring is to prevent the microspine array from being damaged. In pulling grasping

https://doi.org/10.1017/S0263574722000509 Published online by Cambridge University Press

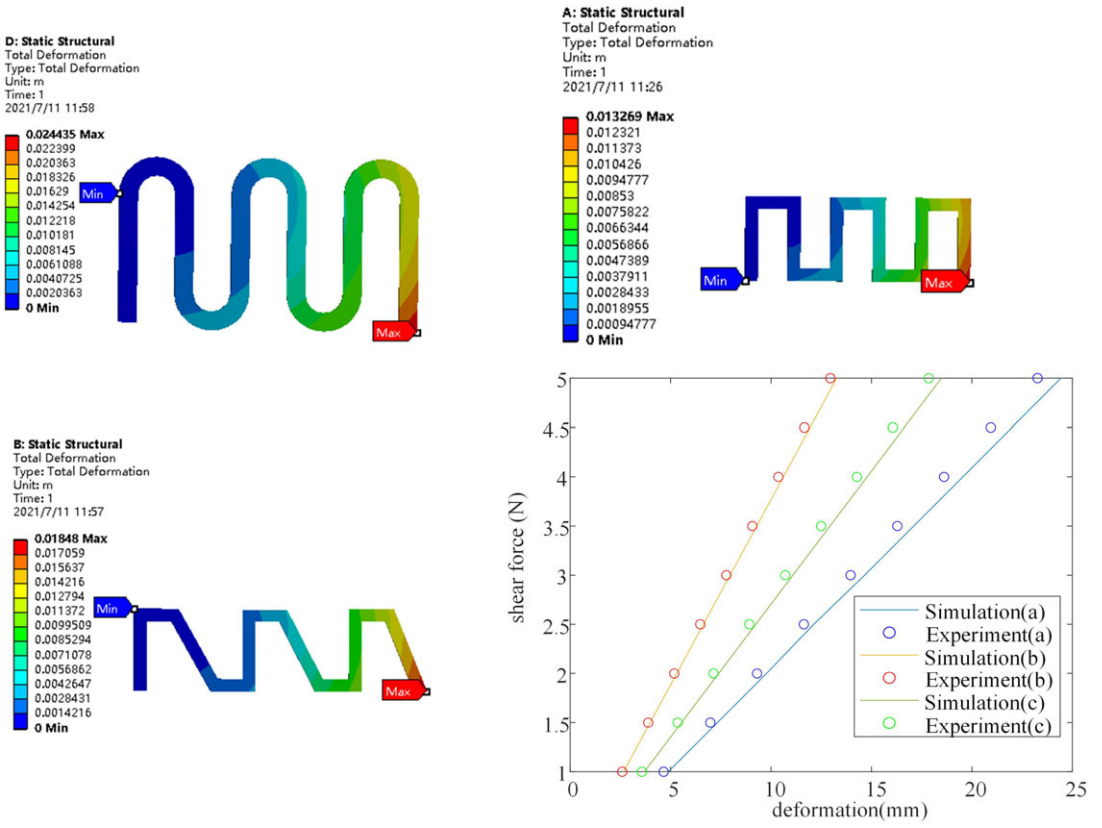

Figure 18. *Deformation and stiffness comparison of microspines.*

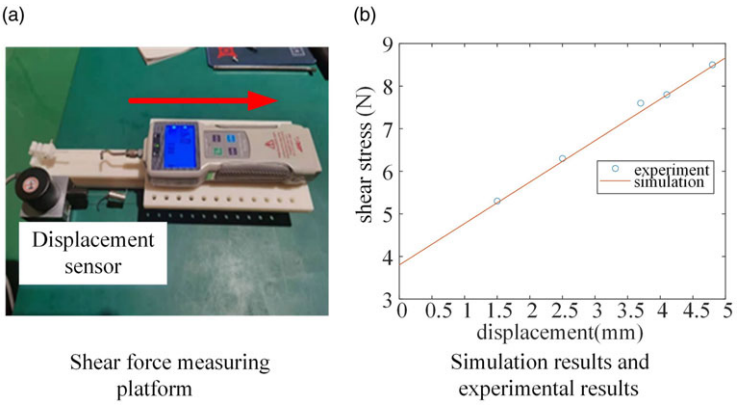

Figure 19. *The microspine stiffness experiment and experimental data.*

mode, the restoring spring is role in pushing the microspine array back to the initial position. According Eq. (22), k_{1x} is the stiffness of the equivalent series spring of the microspine array k_{11x} and the restoring spring k_{12x}. Obviously, the equivalent stiffness can be expressed as:

$$k_{1x} = \frac{1}{\frac{1}{k_{11x}} + \frac{1}{k_{12x}}} \tag{39}$$

https://doi.org/10.1017/S0263574722000509 Published online by Cambridge University Press

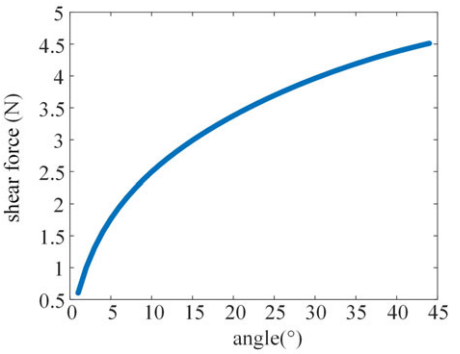

Figure 20. *The relationship between the angle of servo motor and driving force.*

According to Eq. (22), the larger the equivalent stiffness is, the smaller the distance the microspine moves. The equivalent stiffness is less than the minimum of the microspine and the spring. As shown in Fig. 20, the tension provided by the cable nearly reaches the limit after the drive plate rotates 40 degrees.

In pulling sliding mode, the tension provided by the cable compresses the restoring spring first. During this time, the microspine is dragged on the surface to seek the roughness that can be grasped. Once the micropine hooks on the surface, the micropine will form a series spring with the restoring spring, which is the same as the immediate grassing mode. The equivalent stiffness can be expressed as:

$$k_{2x} = \begin{cases} k_{12x}, & x < \delta x \\ k_{1x}, & x \geq \delta x \end{cases} \tag{40}$$

A softer k_{12x} allows the microspine to move longer distances without wasting the pull of the cable. This means that the micropine can go through more roughness, thus increasing the probability of grasping. If k_{12x} is too soft, the attachment unit will need a longer travel to support the load. In the direction perpendicular to the surface, the stiffness of the microspine k_{11y} should be small. The smaller stiffness makes the desorption of the micropine easier, and it will not push the attachment unit away from the wall. k_{12y} has buffering function in both modes. Because the tension of the cable will not cause the attachment unit to rotate around the passive joint when the microspine grasp the surface roughness. However, when the gripper fails to reach the specified position under the guidance of the vision system, the attachment unit rotates to the ground to grasp the ground under the traction of the pulling force. The compressed restoring spring pushes the attachment unit off the ground when the gripper releases the ground. Considering the geometric parameters and design requirements of the gripper, the constraint conditions are as follows:

$$\begin{cases} 1.2k_y < k_{1x} < 4.6k_y \\ \theta_d \leq 30^\circ \\ F_{max} \geq 3N \\ \delta x \leq 15\ \text{mm} \\ \theta \leq 15^\circ \end{cases} \tag{41}$$

The optimization objective is to find the maximum value of global adhesion efficiency index under the constraint conditions. The genetic algorithm is used to solve the constrained extremum problem. Bring the constraint condition into the global adhesion efficiency index to get: $k_{11x} = 1.0618$ Nmm, $k_{12x} = 0.3574$ Nmm, $k_{11y} = 0.6358$ Nmm, $k_{12y} = 0.22784$ mm.

https://doi.org/10.1017/S0263574722000509 Published online by Cambridge University Press

5. Conclusions

In this paper, a novel robot with rigid-flexible coupling girppers for asteroid exploration is proposed. Performance indices based on kinematic model are derived. The relationship between non-dimensional parameters and different performance indices are established. Using the performance atlas method and the genetic algorithm, the dimessional parameters of the robot are optimized. Moreover, the stiffness model of the microspine is established, and thenthe performance index of the global adhesion efficiency is proposed. The genetic algorithm is used to solve the optimal function with respect to the global adhesion efficiency index, and the optimal dimensional parameters of the gripper are obtained. In addition, the stiffness model of the microspine is established to design the stiffness of the microspine and restoring springs. The prototype of the asteroid robot is fabricated and experimental results validate the stiffness model of the microspine and GAEI index proposed in this paper.

Authors' Contributions. QPW was in charge of the whole trial; QPW and JH wrote the manuscript; FG assisted with performance atlas analyses. All authors read and approved the final manuscript.

Authors' Information. Qingpeng Wen, born in 1992, is currently a PhD candidate at *State Key Laboratory of Mechanical Systems and Vibration, School of Mechanical Engineering, Shanghai Jiao Tong University, China*. He received his master degree from *Yanshan University, China*, in 2018. His research interests include mechanism design theory.

Jun He, born in 1981, is currently an associate professor at *State Key Laboratory of Mechanical System and Vibration, Shanghai Jiaotong University, China*. He received his doctoral degree from *Shanghai Jiaotong University, China*, in 2009.

His research interests include mechanism and robotics in space.

Feng Gao, born in 1956, is currently a professor at *State Key Laboratory of Mechanical System and Vibration, Shanghai Jiaotong University, China*. He received his doctoral degree in *Beihang University, China*, in 1991.

Competing Interests. The authors declare no competing financial interests.

Acknowledgements. Not applicable.

Funding. Supported by National Natural Science Foundation of China under Grant No. 52175022, Major Project of Science and Technology Innovation 2030 under Grant No. 2018AAA0102700, the State Key Laboratory of Mechanical System and Vibration under Grant No. MSVZD202106, Key Laboratory Fund of Science and Technology on Space Intelligent Control under Grant No. HTKJ2019KL502011, Shanghai R&D public service platform project Grant No.19DZ2291400.

References

[1] D. E. Trilling, C. Lisse, D. P. Cruikshank, J. P. Emery, Y. Fernández, L. N. Fletcher, D. P. Hamilton, H. B. Hammel, A. W. Harris and M. Mueller, "Spitzer's Solar System studies of asteroids, planets and the zodiacal cloud," *Nat. Astron.* **4**, 940–946 (2020). doi: 10.1038/s41550-020-01221-y.

[2] N. W. Evans and S. A. Tabachnik, "Asteroids in the inner Solar system – II. Observable properties," *Mon. Not. R. Astron. Soc.* **319**, 80–94 (2000). doi: 10.1046/j.1365-8711.2000.03761.x.

[3] J. Kawaguchi, A. Fujiwara and T. Uesug, "Hayabusa - Its technology and science accomplishment summary and Hayabusa-2," *Acta Astronaut.* **62**, 639–647 (2008). doi: 10.1016/j.actaastro.2008.01.028.

[4] A. Fujiwara, J. Kawaguchi, D. K. Yeomans, M. Abe, T. Mukai, T. Okada, J. Saito, H. Yano, M. Yoshikawa and D. J. Scheeres, "The rubble-pile asteroid Itokawa as observed by Hayabusa," *Science* **312**, 1330–1334 (2006). doi: 10.1126/science.1125841.

[5] K. C. Di, Z. Q. Liu, W. H. Wan, M. Peng, B. Liu, Y. Wang, S. Gou and Z. Yue, "Geospatial technologies for Chang'e-3 and Chang'e-4 lunar rover missions," *Geo.-Spat. Inf. Sci.* **23**, 87–97 (2020). doi: 10.1080/10095020.2020.1718002.

[6] M. P. Golombek, H. J. Moore, A. F. C. Haldemann, T. J. Parker and J. T. Schofield, "Overview of the Mars Pathfinder Mission and assessment of landing site predictions," *Science* **278**, 1743–1748 (1997). DOI: 10.1126/science.278.5344.1743.

[7] K. Wittmann, B. Feuerbacher, S. Ulamec, H. Rosenbauer, J. P. Bibring, D. Moura, R. Mugnuolo, S. Dipippo, K. Szego and G. Haerendel, "Rosetta Lander in situ characterization of a comet nucleus," *Acta Astronaut.* **45**, 389–395 (1999). doi: 10.1016/S0094-5765(99)00158-7.

[8] S. Ulamec, S. Espinasse, B. Feuerbacher, M. Hilchenbach, D. Moura, H. Rosenbauer, H. Scheuerle and R. Willnecker, "Rosetta Lander - Philae: Implications of an alternative mission," *Acta Astronaut.* **58**, 435–441 (2006). doi: 10.1016/j.actaastro.2005.12.009.

[9] V. W. Stefaan, T. Yuichi, Y. Kent, M. Akira, T. Satoshi and S. Daniel, "Prearrival deployment analysis of rovers on Hayabusa2 asteroid explorer," *J. Spacecraft Rockets* **55**, 797–817 (2018). doi: 10.2514/1.A34157.

[10] F. Thuillet, P. Michel, C. Maurel, R. L. Ballouz and S. Sugita, "Numerical modeling of lander interaction with a low-gravity asteroid regolith surface Application to MASCOT on board Hayabusa2," *Astron. Astrophys.* **615**, A41 (2018). doi: 10.1051/0004-6361/201832779.
[11] T. M. Ho, V. Baturkin, C. Grimm, J. T. Grundmann and T. Okada, "MASCOT-The mobile asteroid surface scout onboard the Hayabusa2 mission," *Space Sci. Rev.* **208**, 339–374 (2017). doi: 10.1007/s11214-016-0251-6.
[12] L. Fang and F. Gao, "Type design and behavior control for six legged robots," *Chin. J. Mech. Eng.* **31**(1), 48–59 (2018).
[13] K. Uckert, A. Parness, N. Chanover, E. J. Eshelman and P. Boston, "Investigating habitability with an integrated rock-climbing robot and astrobiology instrument suite," *Astrobiology* **20**(12) (2020). doi: 10.1089/ast.2019.2177.
[14] M. Chacin and K. Yoshida, "Stability and Adaptability Analysis for Legged Robots Intended for Asteroid Exploration," **In:** *2006 IEEE/RSJ International Conference on Intelligent Robots and Systems*, Vols. 1–12 (2006) pp. 1744–1749. doi: 10.1109/Iros.2006.282135.
[15] K. Yoshida, T. Maruki and H. Yano, "A novel strategy for asteroid exploration with a surface robot," **In:** *The Second World Space Congress*, vol. 34 (2022) pp. 1966–1971.
[16] J. Hao, E. W. Hawkes, C. Fuller, M. A. Estrada and M. R. Cutkosky, "A robotic device using gecko-inspired adhesives can grasp and manipulate large objects in microgravity," *Sci. Robot.* **2**(7), eaan4545 (2017). doi: 10.1126/scirobotics.aan4545.
[17] D. X. Ge, Y. C. Tang, S. G. Ma, T. Matsuno and C. Ren, "A pressing attachment approach for a wall-climbing robot utilizing passive suction cups," *Robotics* **9**(2), 26 (2020). doi: 10.3390/robotics9020026.
[18] A. Parness, "Anchoring Foot Mechanisms for Sampling and Mobility in Microgravity," **In:** *2011 IEEE International Conference on Robotics and Automation (ICRA)*, San Francisco, USA (2011).
[19] K. Autumn, M. Buehler, M. Cutkosky, R. Fearing, R. J. Full, D. Goldman, R. Groff, W. Provancher, A. A. Rizzi and U. Saranli, "Robotics in Scansorial Environments," **In:** *Unmanned Ground Vehicle Technology Vii*, vol. 5804 (2005) pp. 291–302. doi: 10.1117/12.506157.
[20] S. Wang, H. Jiang, T. M. Huh, D. Sun, W. Ruotolo, M. W. Miller, W. R. T. Roderick, H. Stuart and M. Cutkosky, "SpinyHand: Contact load sharing for a human-scale climbing robot," *J. Mech. Robot. Trans. ASME* **11**(3), 031009 (2019). doi: 10.1115/1.4043023.
[21] A. T. Asbeck and M. R. Cutkosky, "Designing compliant spine mechanisms for climbing," *J. Mech. Robot. Trans. ASME* **4**, 031007 (2012). doi: 10.1115/1.40066591.
[22] A. Parness, M. Frost, J. P. King and N. Thatte, "Demonstrations of Gravity-Independent Mobility and Drilling on Natural Rock Using Microspines," *2012 IEEE International Conference on Robotics and Automation (ICRA)* (2012) pp. 3547–3548.
[23] A. T. Asbeck, S. Kim, M. R. Cutkosky, W. R. Provancher and M. Lanzetta, "Scaling hard vertical surfaces with compliant microspine arrays," *Int. J. Robot. Res.* **25**, 1165–1179 (2006). doi: 10.1177/0278364906072511.
[24] A. Parness, A. Willig, A. Berg, M. Shekels and B. Kennedy, "A Microspine Tool: Grabbing and Anchoring to Boulders on the Asteroid Redirect Mission," **In:** *2017 IEEE Aerospace Conference*, Montana, USA (2017).
[25] S. Q. Wang, H. Jiang and M. R. Cutkosky, "Design and modeling of linearly-constrained compliant spines for human-scale locomotion on rocky surfaces," *Int. J. Robot. Res.* **36**, 985–1000 (2017). doi: 10.1177/0278364917720019.
[26] M. T. Pope, C. W. Kimes, H. Jiang, E. W. Hawkes, M. A. Estrada, C. F. Kerst, W. R. T. Roderick, A. K. Han, D. L. Christensen and M. R. Cutkosky, "A multimodal robot for perching and climbing on vertical outdoor surfaces," *IEEE Trans. Robot.* **33**, 38–48 (2017). doi: 10.1109/Tro.2016.2623346.
[27] G. A. Lynch, J. E. Clark, P. C. Lin and D. E. Koditschek, "A Bioinspired Dynamical Vertical Climbing Robot," *Int. J. Robot. Res.* **31**, 974–996 (2012). doi: 10.1177/0278364912442096.
[28] A. Parness, M. Frost, N. Wiltsie, J. P. King and B. Kennedy, "Gravity Independent Climbing Robot: Technology Demonstration and Mission Scenario Development," **In:** *AIAA SPACE 2013 Conference and Exposition*, San Diego, CA (2013), 8 pp.
[29] R. X. Zhang and J. C. Latombe, "Capuchin: A free-climbing robot invited paper," *Int. J. Adv. Robot. Syst.* **10**, 194 (2013). doi: 10.5772/56469.
[30] J. A. Galvez, J. Estremera and P. G. de Santos, "A new legged-robot configuration for research in force distribution," *Mechatronics* **13**, 907–932 (2003). doi: 10.1016/S0957-4158(03)00008-4.
[31] Z. Liu, H.-C. Zhuang, H.-B. Gao, Z. Q. Deng and L. Ding, "Static force analysis of foot of electrically driven heavy-duty six-legged robot under tripod gait," *Chin. J. Mech. Eng.* **63**(31), 1–15 (2018).
[32] G. D. Wile, K. A. Daltorio, E. D. Diller, L. R. Palmer, S. N. Gorb, R. E. Ritzmann and R. D. Quinn, "Screenbot: Walking Inverted Using Distributed Inward Gripping," **In:** *2008 IEEE/RSJ International Conference on Robots and Intelligent Systems*, Vols. 1–3, Conference Proceedings (2008), p. 1513. doi: 10.1109/Iros.2008.4651045.
[33] X. J. Liu, J. S. Wang and G. Pritschow, "Performance atlases and optimum design of planar 5R symmetrical parallel mechanisms," *Mech. Mach. Theory* **41**, 119–144 (2006). doi: 10.1016/j.mechmachtheory.2005.05.003.
[34] X. J. Liu, J. S. Wang and G. Pritschow, "On the optimal kinematic design of the PRRRP 2-DoF parallel mechanism," *Mech. Mach. Theory* **41**, 1111–1130 (2006). doi: 10.1016/j.mechmachtheory.2005.10.008.
[35] J. Wang, C. Wu and X.-J. Liu, "Performance evaluation of parallel manipulators: Motion/force transmissibility and its index," *Mech. Mach. Theory* **45**, 1462–1476 (2010). doi: 10.1016/j.mechmachtheory.2010.05.001.

Appendix

Table 1. *Some typical results in global optimum region of the leg.*

No.	t_1	t_2	t_3	η_J	$\eta_{J_{\min}}$	η_S	$\eta_{S_{\min}}$
1	1.05	1.1	0.85	0.1933	0.3160	0.0130	0.1361
2	1.05	1.15	0.8	0.1942	0.3161	0.0142	0.1469
3	1.05	1.2	0.75	0.1950	0.3160	0.0155	0.1577
4	1.05	1.35	0.6	0.1964	0.3149	0.0191	0.1895
5	1.05	1.4	0.55	0.1965	0.3143	0.0203	0.1996
6	1.05	1.45	0.5	0.1966	0.3136	0.0214	0.2092
7	1.05	1.5	0.45	0.1965	0.3128	0.0225	0.2182
8	1.05	1.55	0.4	0.1963	0.3120	0.0235	0.2265
9	1.1	1.05	0.85	0.2020	0.3251	0.0128	0.1311
10	1.1	1.1	0.8	0.2031	0.3253	0.0141	0.1423
11	1.1	1.45	0.45	0.2065	0.3232	0.0230	0.2180
12	1.1	1.5	0.4	0.2065	0.3226	0.0241	0.2273
13	1.1	1.55	0.35	0.2064	0.3220	0.0252	0.2358
14	1.15	1.05	0.8	0.2120	0.3342	0.0137	0.1363
15	1.15	1.1	0.75	0.2130	0.3344	0.0151	0.1479
16	1.15	1.3	0.55	0.2158	0.3338	0.0205	0.1937
17	1.15	1.35	0.5	0.2162	0.3335	0.0218	0.2046
18	1.15	1.4	0.45	0.2164	0.3331	0.0231	0.2151
19	1.15	1.45	0.4	0.2166	0.3327	0.0244	0.2250
20	1.15	1.5	0.35	0.2167	0.3323	0.0256	0.2344
21	1.15	1.55	0.3	0.2167	0.3320	0.0267	0.2430
22	1.2	1.05	0.75	0.2220	0.3429	0.0146	0.1409
23	1.2	1.1	0.7	0.2230	0.3430	0.0160	0.1527
24	1.2	1.25	0.55	0.2253	0.3428	0.0203	0.1879
25	1.2	1.3	0.5	0.2259	0.3427	0.0217	0.1992
26	1.2	1.35	0.45	0.2263	0.3424	0.0231	0.2101
27	1.2	1.4	0.4	0.2266	0.3422	0.0244	0.2206
28	1.2	1.45	0.35	0.2269	0.3420	0.0257	0.2304
29	1.2	1.5	0.3	0.2271	0.3419	0.0269	0.2397
30	1.2	1.55	0.25	0.2273	0.3419	0.0280	0.2482
31	1.25	1.05	0.7	0.2320	0.3512	0.0155	0.1450
32	1.25	1.1	0.65	0.2330	0.3513	0.0169	0.1570
33	1.25	1.15	0.6	0.2339	0.3513	0.0184	0.1689
34	1.25	1.2	0.55	0.2347	0.3513	0.0199	0.1807
35	1.25	1.25	0.5	0.2354	0.3513	0.0213	0.1924
36	1.25	1.3	0.45	0.2360	0.3512	0.0228	0.2036
37	1.25	1.35	0.4	0.2365	0.3511	0.0242	0.2145
38	1.25	1.4	0.35	0.2369	0.3511	0.0255	0.2248
39	1.25	1.45	0.3	0.2373	0.3512	0.0269	0.2346
40	1.25	1.5	0.25	0.2377	0.3514	0.0281	0.2437
41	1.3	1.05	0.65	0.2420	0.3590	0.0163	0.1487
42	1.3	1.1	0.6	0.2430	0.3591	0.0178	0.1607
43	1.3	1.3	0.4	0.2461	0.3594	0.0238	0.2072

https://doi.org/10.1017/S0263574722000509 Published online by Cambridge University Press

Table 1. *Continued.*

No.	t_1	t_2	t_3	η_J	$\eta_{J_{\min}}$	η_S	$\eta_{S_{\min}}$
44	1.3	1.35	0.35	0.2467	0.3595	0.0252	0.2180
45	1.3	1.4	0.3	0.2472	0.3598	0.0266	0.2281
46	1.3	1.45	0.25	0.2478	0.3601	0.0279	0.2377
47	1.35	1.05	0.6	0.2517	0.3662	0.0171	0.1519
48	1.35	1.1	0.55	0.2528	0.3663	0.0186	0.1640
49	1.35	1.15	0.5	0.2537	0.3665	0.0202	0.1759
50	1.35	1.3	0.35	0.2561	0.3672	0.0248	0.2101
51	1.35	1.35	0.3	0.2568	0.3676	0.0262	0.2206
52	1.35	1.4	0.25	0.2575	0.3681	0.0276	0.2306
53	1.4	1.05	0.55	0.2612	0.3728	0.0178	0.1546
54	1.4	1.1	0.5	0.2622	0.3730	0.0194	0.1667
55	1.4	1.15	0.45	0.2632	0.3732	0.0210	0.1786
56	1.4	1.2	0.4	0.2641	0.3736	0.0226	0.1902
57	1.4	1.25	0.35	0.2650	0.3740	0.0241	0.2015
58	1.4	1.3	0.3	0.2659	0.3745	0.0257	0.2123
59	1.4	1.35	0.25	0.2668	0.3752	0.0271	0.2225
60	1.45	1.05	0.5	0.2702	0.3786	0.0186	0.1570
61	1.45	1.1	0.45	0.2713	0.3789	0.0202	0.1689
62	1.45	1.15	0.4	0.2723	0.3793	0.0218	0.1808
63	1.45	1.2	0.35	0.2733	0.3798	0.0234	0.1921
64	1.45	1.25	0.3	0.2743	0.3805	0.0250	0.2033
65	1.45	1.3	0.25	0.2754	0.3814	0.0265	0.2138
66	1.5	1.05	0.45	0.2786	0.3836	0.0192	0.1589
67	1.5	1.1	0.4	0.2797	0.3841	0.0209	0.1708
68	1.5	1.15	0.35	0.2808	0.3847	0.0225	0.1824
69	1.5	1.2	0.3	0.2820	0.3855	0.0241	0.1936
70	1.5	1.25	0.25	0.2832	0.3864	0.0257	0.2044
71	1.55	1.05	0.4	0.2862	0.3877	0.0199	0.1606
72	1.55	1.1	0.35	0.2874	0.3884	0.0215	0.1722
73	1.55	1.15	0.3	0.2886	0.3892	0.0232	0.1836
74	1.55	1.2	0.25	0.2899	0.3903	0.0248	0.1946
75	1.6	1.05	0.35	0.2927	0.3908	0.0205	0.1618
76	1.6	1.1	0.3	0.2940	0.3917	0.0221	0.1732
77	1.6	1.15	0.25	0.2954	0.3929	0.0238	0.1844
78	1.65	1.05	0.3	0.2980	0.3929	0.0210	0.1627
79	1.65	1.1	0.25	0.2995	0.3941	0.0227	0.1739
80	1.7	1.05	0.25	0.3018	0.3937	0.0215	0.1633

https://doi.org/10.1017/S0263574722000509 Published online by Cambridge University Press

Table 2. *Some typical results in global optimum region of the multi-legged robot.*

No.	t_b	t_p	t_{leg}	$\eta_{P\min}$	$\eta_{P\max}$	$\eta_{O\min}$	$\eta_{O\max}$	$\mu_{P\min}$	$\mu_{P\max}$	$\mu_{O\min}$	$\mu_{O\max}$	η_{GTI}
1	0.2860	0.9520	1.7620	0.2844	0.4402	0.2353	0.6620	0.1058	0.4671	0.1066	0.7612	0.7564
2	0.2860	0.9580	1.7560	0.2863	0.4458	0.2375	0.6624	0.1065	0.4668	0.1104	0.7613	0.7548
3	0.2860	0.9640	1.7500	0.2881	0.4514	0.2386	0.6627	0.1072	0.4666	0.1144	0.7613	0.7533
4	0.2860	0.9700	1.7440	0.2899	0.4570	0.2422	0.6630	0.1080	0.4664	0.1186	0.7614	0.7517
5	0.2860	0.9760	1.7380	0.2917	0.4625	0.2432	0.6634	0.1087	0.4662	0.1229	0.7614	0.7500
6	0.2860	0.9820	1.7320	0.2935	0.4680	0.2439	0.6637	0.1095	0.4659	0.1273	0.7614	0.7483
7	0.2860	0.9880	1.7260	0.2952	0.4735	0.2441	0.6640	0.1103	0.4657	0.1320	0.7614	0.7466
8	0.2860	0.9940	1.7200	0.2969	0.4789	0.2510	0.6643	0.1110	0.4655	0.1369	0.7614	0.7449
9	0.2860	1.0000	1.7140	0.2986	0.4843	0.2535	0.6647	0.1118	0.4653	0.1419	0.7614	0.7431
10	0.2860	1.0060	1.7080	0.3003	0.4896	0.2541	0.6650	0.1126	0.4651	0.1472	0.7614	0.7413
11	0.2860	1.0120	1.7020	0.3019	0.4949	0.2543	0.6653	0.1134	0.4649	0.1526	0.7613	0.7395
12	0.2860	1.0180	1.6960	0.3036	0.5001	0.2544	0.6657	0.1142	0.4647	0.1583	0.7612	0.7376
13	0.2860	1.0240	1.6900	0.3052	0.5053	0.2545	0.6660	0.1150	0.4645	0.1643	0.7612	0.7357
14	0.2860	1.0300	1.6840	0.3067	0.5104	0.2620	0.6663	0.1158	0.4643	0.1704	0.7611	0.7338
15	0.2860	1.0360	1.6780	0.3083	0.5155	0.2553	0.6666	0.1166	0.4642	0.1768	0.7610	0.7318
16	0.2860	1.0420	1.6720	0.3098	0.5205	0.2554	0.6670	0.1174	0.4640	0.1834	0.7609	0.7298
17	0.2860	1.0480	1.6660	0.3113	0.5255	0.2554	0.6673	0.1182	0.4639	0.1903	0.7607	0.7278
18	0.2860	1.0540	1.6600	0.3128	0.5304	0.2555	0.6676	0.1191	0.4638	0.1975	0.7606	0.7258
19	0.2860	1.0600	1.6540	0.3142	0.5352	0.2556	0.6680	0.1199	0.4637	0.2049	0.7605	0.7237
20	0.2860	1.0660	1.6480	0.3157	0.5400	0.2563	0.6683	0.1208	0.4636	0.2126	0.7603	0.7216
21	0.2860	1.0720	1.6420	0.3171	0.5448	0.2563	0.6686	0.1217	0.4635	0.2205	0.7601	0.7195
22	0.2860	1.0780	1.6360	0.3185	0.5495	0.2586	0.6689	0.1226	0.4634	0.2287	0.7599	0.7174
23	0.2860	1.0840	1.6300	0.3198	0.5541	0.2613	0.6693	0.1234	0.4634	0.2371	0.7597	0.7152
24	0.2860	1.0900	1.6240	0.3212	0.5586	0.2613	0.6696	0.1243	0.4633	0.2457	0.7595	0.7130
25	0.2860	1.0960	1.6180	0.3225	0.5631	0.2614	0.6699	0.1253	0.4633	0.2546	0.7593	0.7108
26	0.2920	0.9520	1.7560	0.2834	0.4362	0.2353	0.6644	0.1068	0.4708	0.1043	0.7606	0.7607
27	0.2920	0.9580	1.7500	0.2853	0.4419	0.2454	0.6656	0.1075	0.4706	0.1081	0.7606	0.7591
28	0.2920	0.9640	1.7440	0.2871	0.4475	0.2455	0.6670	0.1083	0.4704	0.1120	0.7607	0.7576
29	0.2920	0.9700	1.7380	0.2890	0.4531	0.2456	0.6682	0.1090	0.4701	0.1160	0.7607	0.7559

Table 2. *Continued.*

No.	t_b	t_p	t_{leg}	$\eta_{P\min}$	$\eta_{P\max}$	$\eta_{O\min}$	$\eta_{O\max}$	$\mu_{P\min}$	$\mu_{P\max}$	$\mu_{O\min}$	$\mu_{O\max}$	η_{GTI}
30	0.2920	0.9760	1.7320	0.2908	0.4587	0.2457	0.6695	0.1098	0.4699	0.1202	0.7608	0.7543
31	0.2920	0.9820	1.7260	0.2925	0.4642	0.2498	0.6708	0.1106	0.4697	0.1246	0.7608	0.7526
32	0.2920	0.9880	1.7200	0.2943	0.4696	0.2519	0.6721	0.1113	0.4695	0.1292	0.7608	0.7509
33	0.2920	0.9940	1.7140	0.2960	0.4751	0.2520	0.6734	0.1121	0.4693	0.1339	0.7608	0.7492
34	0.2920	1.0000	1.7080	0.2977	0.4805	0.2523	0.6747	0.1129	0.4691	0.1388	0.7608	0.7474
35	0.2920	1.0060	1.7020	0.2994	0.4858	0.2526	0.6760	0.1137	0.4689	0.1440	0.7608	0.7456
36	0.2920	1.0120	1.6960	0.3011	0.4911	0.2603	0.6773	0.1145	0.4687	0.1493	0.7607	0.7437
37	0.2920	1.0180	1.6900	0.3027	0.4963	0.2614	0.6786	0.1153	0.4686	0.1549	0.7607	0.7419
38	0.2920	1.0720	1.6360	0.3163	0.5412	0.2615	0.6799	0.1229	0.4674	0.2156	0.7596	0.7237
39	0.2920	1.0780	1.6300	0.3177	0.5459	0.2616	0.6812	0.1238	0.4673	0.2236	0.7594	0.7216
40	0.2920	1.0840	1.6240	0.3191	0.5506	0.2621	0.6825	0.1247	0.4673	0.2319	0.7592	0.7194
41	0.2920	1.0900	1.6180	0.3204	0.5551	0.2627	0.6838	0.1256	0.4672	0.2403	0.7590	0.7172
42	0.2920	1.0960	1.6120	0.3218	0.5597	0.2629	0.6851	0.1265	0.4672	0.2490	0.7588	0.7149
43	0.2980	0.9520	1.7500	0.2824	0.4322	0.2445	0.6647	0.1078	0.4744	0.1021	0.7599	0.7649
44	0.2980	0.9580	1.7440	0.2843	0.4379	0.2458	0.6647	0.1086	0.4742	0.1057	0.7600	0.7634
45	0.2980	0.9640	1.7380	0.2861	0.4436	0.2472	0.6686	0.1093	0.4740	0.1095	0.7600	0.7618
46	0.2980	0.9700	1.7320	0.2880	0.4492	0.2486	0.6696	0.1101	0.4739	0.1135	0.7601	0.7602
47	0.2980	0.9760	1.7260	0.2898	0.4548	0.2499	0.6711	0.1109	0.4737	0.1176	0.7601	0.7585
48	0.2980	0.9820	1.7200	0.2916	0.4603	0.2513	0.6723	0.1117	0.4735	0.1219	0.7602	0.7569
49	0.2980	0.9880	1.7140	0.2934	0.4658	0.2527	0.6736	0.1124	0.4733	0.1263	0.7602	0.7551
50	0.2980	0.9940	1.7080	0.2951	0.4712	0.2540	0.6749	0.1132	0.4731	0.1310	0.7602	0.7534
51	0.2980	1.0000	1.7020	0.2968	0.4766	0.2554	0.6762	0.1140	0.4729	0.1358	0.7602	0.7516
52	0.2980	1.0060	1.6960	0.2985	0.4820	0.2568	0.6775	0.1148	0.4728	0.1408	0.7602	0.7498
53	0.2980	1.0120	1.6900	0.3002	0.4873	0.2581	0.6788	0.1156	0.4726	0.1460	0.7601	0.7480
54	0.2980	1.0660	1.6360	0.3142	0.5329	0.2595	0.6801	0.1232	0.4714	0.2033	0.7592	0.7300
55	0.2980	1.0720	1.6300	0.3156	0.5376	0.2609	0.6814	0.1241	0.4713	0.2108	0.7591	0.7279
56	0.2980	1.0780	1.6240	0.3170	0.5424	0.2622	0.6826	0.1250	0.4713	0.2187	0.7589	0.7257

Table 2. *Continued.*

No.	t_b	t_p	t_{leg}	$\eta_{P\min}$	$\eta_{P\max}$	$\eta_{O\min}$	$\eta_{O\max}$	$\mu_{P\min}$	$\mu_{P\max}$	$\mu_{O\min}$	$\mu_{O\max}$	η_{GTI}
57	0.2980	1.0840	1.6180	0.3184	0.5470	0.2636	0.6839	0.1259	0.4712	0.2268	0.7587	0.7235
58	0.2980	1.0900	1.6120	0.3197	0.5516	0.2650	0.6852	0.1268	0.4712	0.2351	0.7585	0.7213
59	0.2980	1.0960	1.6060	0.3211	0.5562	0.2663	0.6865	0.1278	0.4712	0.2436	0.7583	0.7191
60	0.3040	0.9520	1.7440	0.2813	0.4282	0.2543	0.6727	0.1088	0.4779	0.0999	0.7592	0.7692
61	0.3040	0.9580	1.7380	0.2832	0.4339	0.2572	0.6733	0.1096	0.4778	0.1035	0.7593	0.7676
62	0.3040	0.9640	1.7320	0.2851	0.4396	0.2601	0.6756	0.1104	0.4777	0.1072	0.7594	0.7660
63	0.3040	0.9700	1.7260	0.2870	0.4452	0.2631	0.6767	0.1111	0.4775	0.1110	0.7594	0.7644
64	0.3040	0.9760	1.7200	0.2888	0.4508	0.2660	0.6782	0.1119	0.4774	0.1151	0.7595	0.7628
65	0.3040	0.9820	1.7140	0.2906	0.4564	0.2689	0.6796	0.1127	0.4772	0.1193	0.7595	0.7611
66	0.3040	0.9880	1.7080	0.2924	0.4619	0.2718	0.6811	0.1135	0.4770	0.1236	0.7596	0.7594
67	0.3040	0.9940	1.7020	0.2942	0.4674	0.2747	0.6825	0.1143	0.4769	0.1281	0.7596	0.7576
68	0.3040	1.0000	1.6960	0.2959	0.4728	0.2776	0.6840	0.1151	0.4767	0.1328	0.7596	0.7558
69	0.3040	1.0300	1.6660	0.3042	0.4992	0.2805	0.6854	0.1193	0.4760	0.1594	0.7594	0.7464
70	0.3040	1.0360	1.6600	0.3058	0.5044	0.2834	0.6869	0.1201	0.4759	0.1653	0.7593	0.7445
71	0.3040	1.0420	1.6540	0.3074	0.5095	0.2863	0.6883	0.1210	0.4757	0.1715	0.7592	0.7425
72	0.3040	1.0480	1.6480	0.3089	0.5145	0.2892	0.6898	0.1218	0.4756	0.1780	0.7591	0.7404
73	0.3040	1.0540	1.6420	0.3104	0.5195	0.2921	0.6912	0.1227	0.4755	0.1846	0.7590	0.7384
74	0.3040	1.0600	1.6360	0.3119	0.5244	0.2951	0.6927	0.1236	0.4754	0.1916	0.7589	0.7363
75	0.3040	1.0660	1.6300	0.3134	0.5292	0.2980	0.6941	0.1245	0.4753	0.1987	0.7587	0.7342
76	0.3040	1.0720	1.6240	0.3148	0.5340	0.3009	0.6956	0.1253	0.4753	0.2062	0.7586	0.7320
77	0.3040	1.0780	1.6180	0.3162	0.5388	0.3034	0.6970	0.1263	0.4752	0.2138	0.7584	0.7298
78	0.3040	1.0840	1.6120	0.3176	0.5435	0.3054	0.6985	0.1272	0.4751	0.2217	0.7582	0.7276
79	0.3040	1.0900	1.6060	0.3190	0.5481	0.3077	0.6999	0.1281	0.4751	0.2299	0.7580	0.7254
80	0.3040	1.0960	1.6000	0.3203	0.5527	0.3107	0.7013	0.1290	0.4751	0.2382	0.7578	0.7232

Cite this article: Q. Wen, J. He and F. Gao (2022). "Kinematic design of a novel Multi-legged robot with Rigid-flexible coupling grippers for asteroid exploration", Robotica **40**, 3699–3725. https://doi.org/10.1017/S0263574722000509